PHYSICAL REVIEW C **87**, 014908 (2013)

Narrowing the uncertainty on the total charm cross section and its effect on the J/ψ cross section

R. E. Nelson,[1,2] R. Vogt,[1,2] and A. D. Frawley[3]
[1]*Physics Division, Lawrence Livermore National Laboratory, Livermore, California 94551, USA*
[2]*Physics Department, University of California at Davis, Davis, California 95616, USA*
[3]*Physics Department, Florida State University, Tallahassee, Florida 32306, USA*

(Received 14 September 2012; published 22 January 2013)

We explore the available parameter space that gives reasonable fits to the total charm cross section to make a better estimate of its true uncertainty. We study the effect of the parameter choices on the energy dependence of the J/ψ cross section.

DOI: 10.1103/PhysRevC.87.014908 PACS number(s): 12.38.Bx, 14.65.Dw, 25.75.Cj

I. INTRODUCTION

Because the charm quark mass is finite, the total charm production cross section can be calculated in perturbative QCD. However, the charm quark mass is relatively light so that there are large uncertainties owing to the choice of quark mass, factorization scale, and renormalization scale [1]. Typical lower limits of the factorization and renormalization scales are half the chosen charm quark mass [1,2]. Here, the parton densities are subject to backward evolution, as the factorization scale is below the minimum scale of the parton densities. In addition, for renormalization scales below 1 GeV, the strong coupling constant α_s becomes large and the perturbative expansion is unlikely to converge. Thus it is worth evaluating our assumptions concerning these parameters to determine whether we can find a set of physically defensible mass and scale parameters that reduce the cross section uncertainty.

In the color evaporation model (CEM) of J/ψ production, the J/ψ cross sections are calculated with the same set of mass and scale parameters as open charm production [3]. As we will show, the parameters used to calculate the uncertainty on the charm quark cross sections in Refs. [1,2] do not place stringent bounds on the J/ψ production cross section. We therefore seek to place limits on the J/ψ cross section calculated in the CEM for the first time.

In this paper we explore the charm quark mass and scale parameter space to reduce the uncertainty in the charm total cross section. In Sec. II, we use existing data to set limits on the factorization and renormalization scales. We then calculate the lepton distributions from heavy-flavor decays with our parameter limits and compare them to data from the Relativistic Heavy Ion Collider (RHIC) and the Large Hadron Collider (LHC) as a reality check. Section III describes how we use our open charm results in CEM calculations of J/ψ production to determine the uncertainties on quarkonium production, both as a function of incident energy and as a function of the kinematic variables. In Sec. IV, we summarize our results.

II. SETTING LIMITS ON THE TOTAL CHARM CROSS SECTION

In our previous efforts to place uncertainties on the total charm cross section using the same fiducial parameter set as the fixed-order next-to-leading logarithm (FONLL) calculation, we found a wide uncertainty band that grew larger at high center-of-mass energies [1,4]. At high energies, the lower limit was determined by a factorization scale of half the central value of the charm quark mass, assumed to be 1.5 GeV. In this region, the behavior of the gluon density at low momentum fraction, x, when the parton densities are backwards evolved caused the cross section to grow unphysically slowly with energy. The upper limit of the uncertainty is obtained when the renormalization scale is equal to half the charm quark mass. Here the two-loop evaluation of the strong coupling constant gives $\alpha_s > 0.5$, too large for convergence of the perturbative expansion. In this work we use the total charm cross section data to obtain a more physically motivated set of parameters for charm production.

We calculate the total hadronic charm production cross section in a pp collision directly using the next-to-leading-order (NLO) matrix elements [5] for the total partonic cross section, $\hat{\sigma}$,

$$\sigma_{AB}(\sqrt{s}, m^2) = \sum_{i,j=q,\overline{q},g} \int dx_1\, dx_2\, f_i^p\left(x_1, \mu_F^2\right) \times f_j^p\left(x_2, \mu_F^2\right) \widehat{\sigma}_{ij}\left(\hat{s}, m^2, \mu_F^2, \mu_R^2\right), \quad (1)$$

where m is the charm quark mass, μ_F is the factorization scale, μ_R is the renormalization scale, $\sqrt{s}$ is the partonic center-of-mass energy, x_1 and x_2 are the fractions of the parent proton's momenta carried by the colliding partons, and f_i^p are the proton parton densities. The NLO calculation remains the state of the art for the total cross section; there is still no complete next-to-next-to-leading-order (NNLO) evaluation of the total cross section, especially at energies where $\sqrt{s} \gg m$. We use the central CT10 parton density set [6] but also show the variation in the cross section based on all 52 variants of the Hessian uncertainty matrix.

Because Eq. (1) is independent of the heavy-quark kinematics, it is typical to take $\mu_{R,F} = m$ as the central value and vary the two scales independently within a "fiducial" region defined by $\mu_{R,F}/m$ with $0.5 \leqslant \mu_{R,F}/m \leqslant 2$ and $0.5 \leqslant \mu_R/\mu_F \leqslant 2$. In earlier work, we used the following seven sets: $\{(\mu_F/m, \mu_R/m)\} = \{(1,1), (2,2), (0.5,0.5), (1,0.5), (2,1), (0.5,1), (1,2)\}$ [1,2]. The uncertainties from the mass variation and the combined scale variations listed above were then added in quadrature. The envelope containing the resulting curves,

$$\sigma_{\max} = \sigma_{\rm cent} + \sqrt{(\sigma_{\mu,\max} - \sigma_{\rm cent})^2 + (\sigma_{m,\max} - \sigma_{\rm cent})^2}, \qquad (2)$$

$$\sigma_{\min} = \sigma_{\rm cent} - \sqrt{(\sigma_{\mu,\min} - \sigma_{\rm cent})^2 + (\sigma_{m,\min} - \sigma_{\rm cent})^2}, \qquad (3)$$

defines the uncertainty in the total cross section as a function of the center-of-mass energy. Here $\sigma_{\rm cent}$ is the cross section calculated with the central set, $(\mu_F/m, \mu_R/m) = (1, 1)$ and $m = 1.5$ GeV, while $\sigma_{i,\max}$ and $\sigma_{i,\min}$ are the maximum and minimum values of the cross section for a given mass ($i = m$) or $(\mu_F/m, \mu_R/m)$ set in the fiducial region ($i = \mu$). Although Eqs. (2) and (3) have been written for the total cross section, the corresponding maximum and minimum values of the differential distributions can be written similarly [2].

The charm quark mass we employ in our calculations is the Particle Data Group (PDG) value based on lattice determinations of the charm quark mass in the $\overline{\rm MS}$ scheme at $\mu = m$: $m(m) = 1.27 \pm 0.09$ GeV [7]. The fiducial $c\bar{c}$ parameter sets used in FONLL calculations [2] employ a higher charm quark mass, $m = 1.5$ GeV. None of these fiducial parameter sets give a particularly good fit to the total charm data. When $n_f = 3$ flavors are used, as is proper for charm production, there is a wide uncertainty band on $\sigma_{\rm tot}$, especially at the center-of-mass energies appropriate for colliders, $\sqrt{s} > 200$ GeV, primarily owing to unconstrained gluon densities at low x for $\mu_F/m = 0.5 \leqslant \mu_0/m$, where μ_0 is the minimum scale of the parton densities. Previous calculations with lower charm quark masses but higher scales [8] agree better with data while avoiding backward evolution of the gluon density at low x. This bias of lower masses with higher scales allows us to reduce the uncertainty in the charm production cross section.

In principle, fitting the data is somewhat problematic, as we neglect unknown next-order uncertainties. This is particularly true for charm, where the mass is relatively small and $\mathcal{O}(\alpha_s^4)$ corrections could be large. Indeed, approximate NNLO calculations show that, while the scale dependence is reduced, the K factor between the approximate NNLO and the NLO results is similar to that between the NLO and the leading-order calculations [9,10]. Because a full NNLO calculation is not yet available, we feel that a fit that narrows the uncertainties at collider energies is useful, keeping in mind that a full NNLO calculation might yield a good fit to the data with higher masses and somewhat lower scales.

For a fixed charm quark mass, we fit the factorization and renormalization scale parameters to a subset of the total charm production data. We use part of the fixed-target data measured with incident protons at beam energies $E_{\rm beam} = 250$ GeV [11], 360 GeV [12], 400 GeV [13], 450 GeV [14], 800 GeV [15,16], and 920 GeV [17]. We do not include incident pion data in the analysis because there have been no new global analyses of the pion parton densities since 1999 [18] and none of the past pion fits are compatible with modern proton parton densities. The Lexan bubble chamber (LEBC) was used in the measurements of the NA16 [12], NA27 [13], and E743 [15] collaborations. The LEBC allowed direct observation of the charm production and decay vertices. The first two measurements were made at CERN [12,13], while the last was made at Fermilab [15]. The 800 GeV E653 measurement at Fermilab used an emulsion target to measure the primary production vertex and at least one decay vertex contained within the emulsion volume [16]. While none of these experiments had very high statistics, their results were very clean. The E769 Collaboration used silicon vertex detectors to reconstruct D meson ($D^\pm$, $D^0/\overline{D}^0$, and $D_s^\pm$) decays [11]. The NA50 data at $E_{\rm beam} = 450$ GeV were obtained by studying the lepton pair invariant mass continuum over a range of nuclear targets. The continuum was assumed to be a superposition of dimuons from the Drell-Yan process and semileptonic decays of open charm. Because the A dependence of open charm and Drell-Yan production is compatible with a linear growth, $\sigma_{pA} = \sigma_{pp}A$, the charm cross section was obtained from a global fit to the four targets studied (Al, Cu, Ag, and W) [14]. The data from Refs. [11–13,15,16] were evaluated in the review by Lourenço and Wöhri and adjusted to the values we employ in our fits using the most up-to-date branching ratios for the measured decay channels [19].

We also include total cross section data at $\sqrt{s} = 200$ GeV from RHIC. There are data from both PHENIX [20] and STAR [21–23]. The PHENIX measurement is based on inclusive single-electron p_T distributions in pp collisions in the pseudorapidity interval $|\eta| < 0.35$. The "nonphotonic" electrons, assumed to come from heavy-flavor decays, were extracted from the total electron spectrum by subtracting "photonic" (background) sources. The shape of the resulting p_T distribution is described by a superposition of charm and bottom contributions. The charm contribution was extrapolated to $p_T = 0$ to obtain the total charm cross section, $0.551^{+0.203}_{-0.231}$ mb [20]. The first STAR data point was extracted from $d+$Au collisions by two independent measurements [21]. They directly reconstructed $D^0 \to K^+\pi^-$ decays with $|y| < 1$ and $0.1 < p_T < 3$ GeV. STAR also used inclusive non-photonic electrons to study semileptonic decays of charm. The initial result, $1.4 \pm 0.2 \pm 0.4$ mb [21], was significantly higher than the PHENIX result but compatible within systematic uncertainties. After a reanalysis of the nonphotonic electron data and new D meson measurements, the STAR cross section reported at Quark Matter 2011 came down to 0.949 ± 0.365 mb [22], while the final result, obtained after our analysis was finished, is reduced to $0.797 \pm 0.210^{+0.208}_{-0.262}$ mb [23]. While the final STAR result is still higher than the PHENIX cross section, the two results are now comparable within uncertainties.

We have made five different fits to combinations of the data just described: using the fixed-target data [11–13,15–17] only; adding only the PHENIX data [20]; adding the PHENIX and the 2004 STAR result [21]; and, finally, including the 2011 STAR result [22] and, subsequently, checking how much the results changed when the final 2012 STAR point [23] was added to the PHENIX data. The experimental uncertainties used in the fitting were obtained by adding the statistical and systematic uncertainties in quadrature.

In our analysis, the total charm cross sections were calculated for a range of charm quark masses between 1.18 and

TABLE I. Factorization, μ_F/m, and renormalization, μ_R/m, scale uncertainties obtained by fitting subsets of the total charm cross section data with $m = 1.27$ GeV.

Fitted data	μ_F/m	μ_R/m	χ^2/dof
Fixed target only	$1.1^{+1.00}_{-0.40}$	$1.6^{+0.13}_{-0.08}$	1.03
+PHENIX	$1.6^{+1.53}_{-0.56}$	$1.6^{+0.09}_{-0.13}$	1.03
+STAR (2004)	$2.8^{+2.73}_{-1.35}$	$1.6^{+0.14}_{-0.10}$	1.53
+STAR (2011)	$2.1^{+2.55}_{-0.85}$	$1.6^{+0.11}_{-0.12}$	1.16
+STAR (2012)	$2.1^{+2.21}_{-0.79}$	$1.6^{+0.10}_{-0.11}$	1.06

1.54 GeV in steps of 0.03 GeV. At each mass, we varied μ_F/m between 0.45 and 10.65 while simultaneously varying μ_R/m between 0.5 and 2.9. The step size in μ_F/m and μ_R/m was 0.05 in both cases. The χ^2/dof (degrees of freedom) for each parameter set was evaluated by comparing the calculated cross sections with each of the five subsets of the data considered.

The best-fit values of μ_F/m and μ_R/m are rather sensitive to the charm mass. In general, increasing the quark mass above 1.27 GeV decreases both μ_F/m and μ_R/m. It also tends to increase the χ^2/dof for each fit. If one plots χ^2/dof for a given value of m as a function of either μ_F/m or μ_R/m while the other scale parameter is held fixed, typical parabolic shapes with a minimum are found. The parabolas grow narrower as the mass increases. When $m \leqslant 1.2$ GeV, single-variable parabolas of χ^2/dof are rather broad and prefer high $\mu_{R,F}/m$ values. For $m \geqslant 1.5$ GeV, the fits give $\mu_{F,R}/m \leqslant 1$, close to the minimum μ_F of the parton densities and in a region where $\alpha_s(\mu_R^2)$ is rather large.

Because the charm quark mass was assigned the value of $m = 1.27 \pm 0.09$ GeV by the PDG, we decided to add a penalty to the χ^2 equal to $(m - m_{\rm PDG})^2/\Delta m_{\rm PDG}^2$. With this penalty for deviations from the PDG value of the charm quark mass, the minimum χ^2/dof when varying the charm quark mass within our chosen range was found for $m = 1.27$ GeV, the PDG mass, for all five subsets of the data.

The best-fit results in all cases are listed in Table I. The χ^2/dof for each fit is also reported. The largest χ^2/dof is obtained when the 2004 STAR point is used, as it is high relative to the $\sqrt{s}$ dependence of the other measurements. We note that the values of μ_F/m found with the later STAR results is more in line with physical arguments than those obtained with the 2004 data.

The uncertainties in the fitted parameters were evaluated from the χ^2 distributions. We show the χ^2 fit contours in Fig. 1 for the four cases represented in Table I. The χ^2 contours in μ_F/m (x axis) and μ_R/m (y axis) are depicted at $\Delta\chi^2 = 0.3$, 1, and 2.3. The one standard deviation, $1\sigma_\chi$, uncertainty in the fitted value of μ_F/m (μ_R/m) was taken as the maximum extent of the $\Delta\chi^2 = 1$ contour along the μ_F/m (μ_R/m) axis. These uncertainties are included with the best-fit parameter values in Table I. The $1\sigma_\chi$ uncertainty in the total cross section is the range of cross sections resulting from all combinations of μ_F/m and μ_R/m contained within the $\Delta\chi^2 = 2.3$ contour. The $\Delta\chi^2 = 0.3$ contour is included only to guide the eye.

Using the final STAR data point [23] in the fitting does not change the optimum values of the scale parameters, μ_F/m and μ_R/m. It only changes the $1\sigma_\chi$ limits on the scale parameters. The upper and lower limits on μ_F/m are reduced by 8% and 4%, respectively, while the limits in μ_R/m change by less than 1% (see Table I). Because the analysis for this paper was completed before the latest STAR charm data release, we used the limits obtained with the preliminary point in our further analysis.

Note the narrow range in μ_R/m relative to the much broader μ_F/m range, even for fits to the fixed-target data only. Indeed, the largest difference in the fits to the various data sets is in the μ_F/m range. The μ_F/m range compatible with the data varies considerably for the different fits; note the difference in μ_F/m ranges for Figs. 1(a)–1(d). The fixed-target data probe a region of relatively large parton momentum fractions, $x \sim 2m/\sqrt{s}$, equivalent to $0.06 < x < 0.12$ for $19.4 \leqslant \sqrt{s} \leqslant 40$ GeV. This range of x is near the pivot point of the gluon distribution, $xg(x, \mu_F^2)$, as a function of x for a range of factorization scales. The fixed-target data are therefore rather insensitive to the evolution of the gluon density as a function of μ_F so that the results skew toward rather low values of μ_F/m.

Including RHIC data in the fit introduces greater sensitivity to the low-x region, although $x \sim 0.012$ at midrapidity is near the high-x edge of the low-x regime. The PHENIX point, obtained earliest, has the lowest cross section and thus requires a lower factorization scale than when either of the two STAR points is included. The STAR cross section from 2004, more than a factor of two larger than the PHENIX cross section, requires the largest factorization scale of all the fits. Note the high value, $\mu_F/m \sim 10$, required to close the $\Delta\chi^2 = 2.3$ contour for this fit. The newer STAR measurements [22,23], based on reconstructed D meson decays in pp collisions, rather than on d + Au collisions, gives a lower best-fit value of μ_F/m than the 2004 cross section but still higher than that either with the fixed-target data only or with only the PHENIX measurement at 200 GeV.

The value of μ_F/m is strongly dependent on the data sets used in the fits. The uncertainty in μ_F/m is very asymmetric, with a 100% or greater upper uncertainty relative to the best-fit value. The difference between the lower limit of the uncertainty in μ_F/m and the best-fit value is not as large because there is a much greater change in $xg(x, \mu_F^2)$ at lower factorization scales than when $\mu_F \gg \mu_0$. Finally, we note that the value of μ_F/m has the greatest effect on the energy dependence of the total charm cross section.

The best-fit value of μ_R/m is the same in all cases and the uncertainty is much smaller than for μ_F/m. These uncertainties are also asymmetric but they typically differ by less than 10%, indicating that μ_R/m acts to fine-tune the magnitude of the cross section. Changing μ_R/m changes the total cross section by the same factor at all energies and does not affect the energy dependence of the cross section.

Figure 2 shows the resulting energy dependence of the total charm cross section for the four different fits and the corresponding uncertainty based on results using the $1\sigma_\chi$ uncertainties in the quark mass and scale parameters. If the central, upper, and lower limits of $\mu_{R,F}/m$ are denoted C, H, and L, respectively, then the seven sets corresponding to the "fiducial" region are $\{(\mu_F/m, \mu_F/m)\} = \{(C, C), (H, H), (L, L), (C, L), (L, C), (C, H), (H, C)\}$. The upper and lower

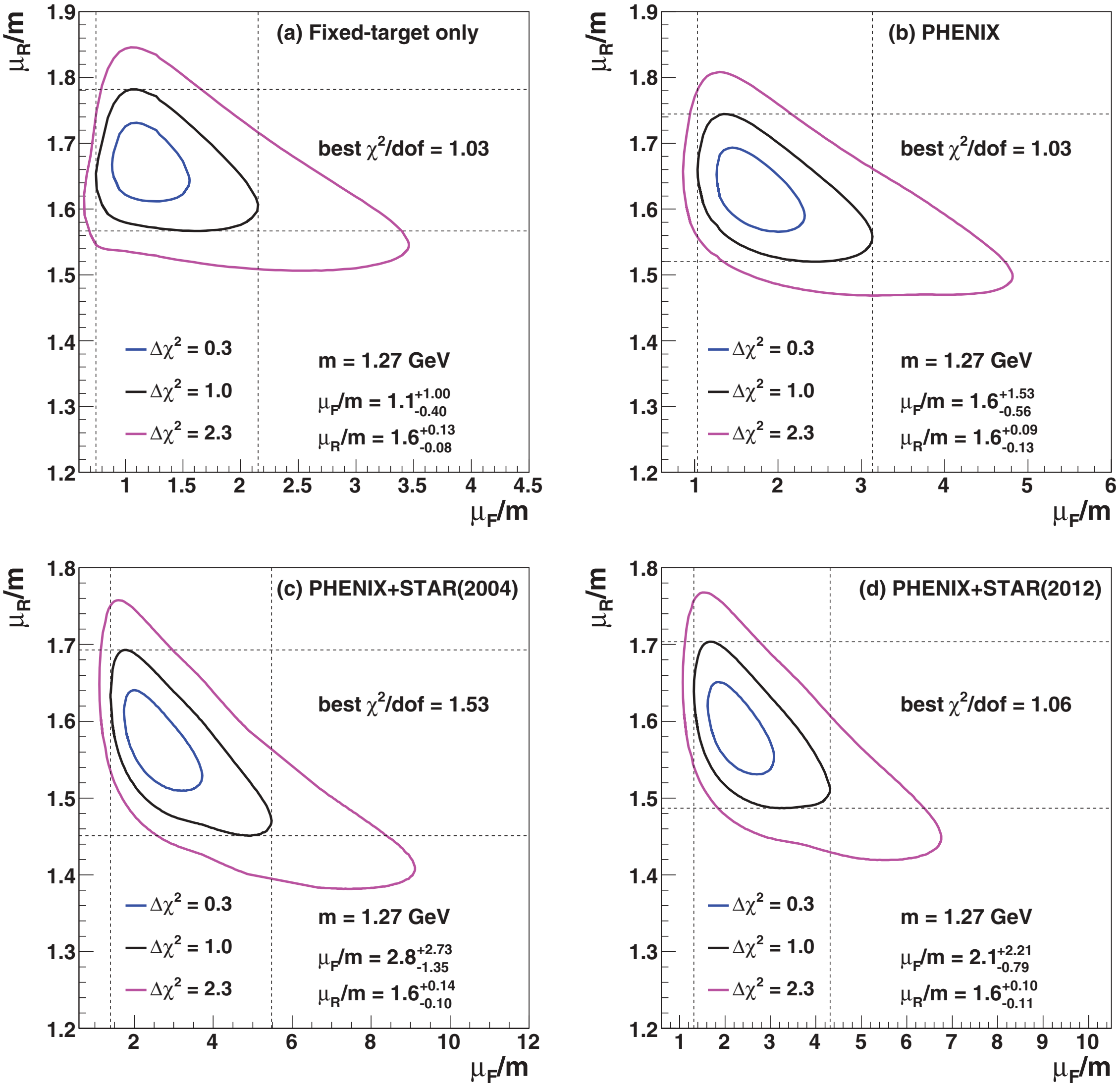

FIG. 1. (Color online) The χ^2/dof contours for (a) fixed-target data only, (b) data including the PHENIX 200 GeV cross section, (c) data including the STAR 2004 cross section, and (d) data including the STAR 2012 cross section but excluding the STAR 2004 cross section. Best-fit values are given for the furthest extent of the $\Delta\chi^2 = 1$ contours. Note that while the y-axis range is the same in all four panels, the x-axis range varies significantly.

limits in the PDG value of the charm quark mass are 1.36 and 1.18 GeV. The uncertainty band can be obtained for the best-fit sets using Eqs. (2) and (3). The uncertainty bands are shown for two cases: the regular fiducial region and with inclusion of the most extreme cases $(\mu_F/m, \mu_R/m) = (H, L)$ and (L, H). These two combinations give the most extreme values of the cross section because the maximum value of μ_F/m produces the fastest evolution of the parton densities, while the minimum value of μ_R/m results in the largest values of the strong coupling constant with $(\mu_F/m, \mu_R/m) = (H, L)$; the opposite is true for $(\mu_F/m, \mu_R/m) = (L, H)$. The difference between the outer dashed (magenta) curves, which include these extremes, and the dot-dashed (cyan) curves, which do not, is very small. Therefore, it is reasonable to neglect the effect of these extremes.

Note that the fits all result in an asymmetric uncertainty band for $\sqrt{s} \geqslant 100$ GeV. This arises because the uncertainty in the fits of μ_F/m is asymmetric (see Table I), with the upper value significantly higher than the lower. As μ_F increases so that $\mu_F \gg \mu_0$, the evolution of the gluon density with μ_F is reduced for the upper limit of μ_F/m. However, the closer the lower limit of the fitted μ_F is to μ_0, the stronger the factorization scale evolution of the gluon density becomes, giving a greater difference between the central value of μ_F/m and the lower limit than between the central value and the upper limit.

All the fit results shown in Fig. 2 agree equally well with the fixed-target data. However, the fit to the fixed-target data alone gives the lowest cross sections at collider energies, $\sqrt{s} \geqslant 200$ GeV. The low factorization scale values result in a slowing of the growth of the total cross section. The narrowest uncertainty band is obtained when the 2004 STAR measurement is used in the fit because it requires the largest factorization scale. Despite this, the top of the calculated uncertainty band does not even touch the bottom of the

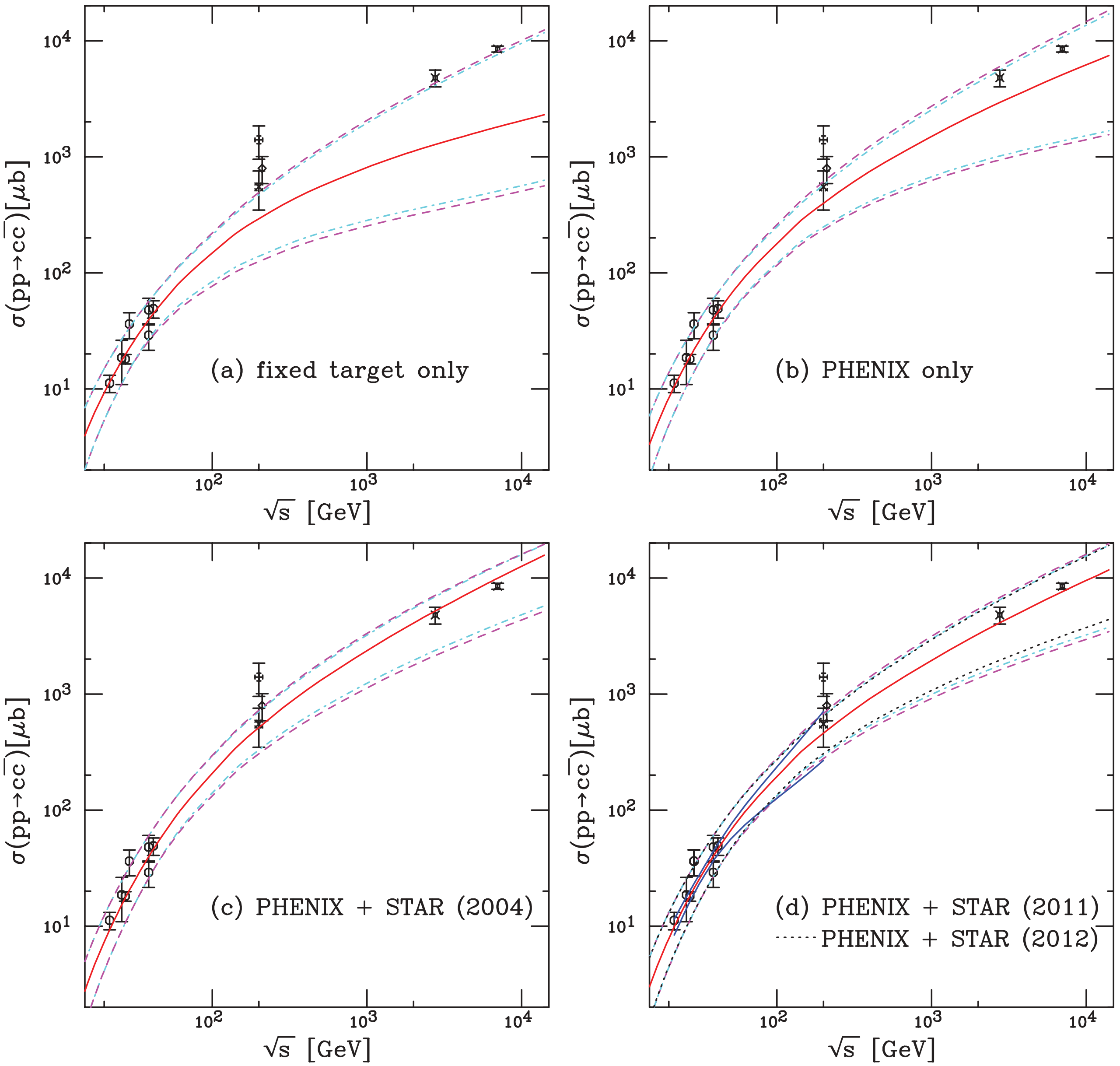

FIG. 2. (Color online) Energy dependence of the charm total cross section compared to data for the fits to (a) fixed target data only, (b) data including the PHENIX 200 GeV cross section, (c) data including the STAR 2004 cross section, and (d) data including the STAR 2011 cross section but excluding the STAR 2004 cross section. Best-fit values are given for the furthest extent of the $\Delta\chi^2 = 1$ contours. The central value of the fit in each case is given by the solid (red) curve while the dashed (magenta) curves and dot-dashed (cyan) curves show the extent of the corresponding uncertainty bands. Dashed curves outline the most extreme limits of the band. In (d), the dotted (black) curves show the uncertainty bands obtained with the 2012 STAR results, while the solid (blue) curves, in the range $19.4 \leqslant \sqrt{s} \leqslant 200$ GeV, represent the uncertainty obtained from the extent of the $\Delta\chi^2 = 2.3$ contour in Fig. 1(d).

uncertainty in measurement. On the other hand, the most recent STAR measurements are compatible with the upper limits of the uncertainty in the fit values. The stronger growth in the energy dependence of the total cross section when the RHIC data are included is attributable to the requirement of a larger value of μ_F/m to fit the data, steepening the slope of the energy dependence at large $\sqrt{s}$. The dot-dashed and dashed curves in Fig. 2(d) were calculated with the preliminary STAR 2011 point [22]. The dotted (black) curves in Fig. 2(d) show the limits on the cross sections calculated using the final STAR value [23]. The difference in the calculated upper limits is 0.77% at 200 GeV and 0.70% at 7 TeV, while the difference in the lower limits is −3.36% at 200 GeV and −12.65% at 7 TeV. There is a smaller difference in the upper limits owing to the relatively smaller changes in the gluon distributions at low x, high μ_F, compared to low x, low μ_F.

Finally, in Fig. 2(d) we also show the result for a $1\sigma_\chi$ uncertainty in the total cross section obtained from the $\Delta\chi^2 = 2.3$ contour in Fig. 1. The resulting band is narrower than the uncertainty band obtained from the scale uncertainties

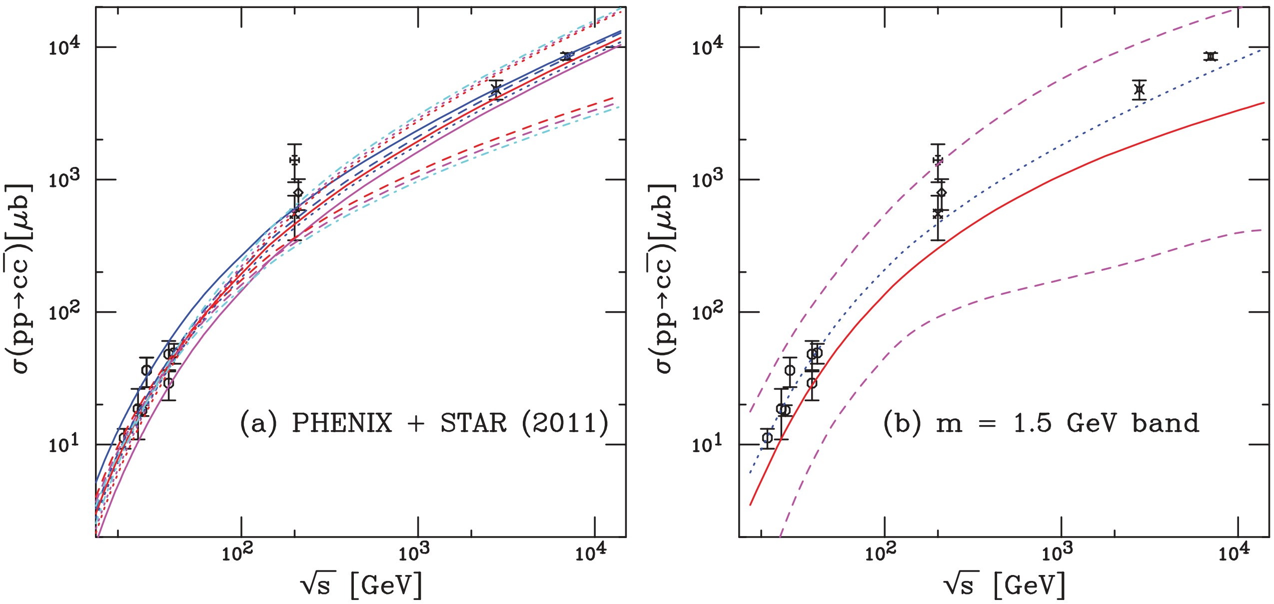

FIG. 3. (Color online) (a) Components of the uncertainty band in Fig. 2(d). The central value $(m, \mu_F/m, \mu_R/m) = (1.27$ GeV, 2.10, 1.60) is shown by the solid red curve. The solid blue and magenta curves outline the mass uncertainty with (1.18 GeV, 2.10, 1.60) and (1.36 GeV, 2.10, 1.60), respectively. Dashed curves outline the lower limits on the scale uncertainty: $(\mu_F/m, \mu_R/m) = (2.10, 1.48)$ blue; (1.25, 1.60) magenta; and (1.25, 1.48) red. Dotted curves outline the upper limits on the scale uncertainty: $(\mu_F/m, \mu_R/m) = (2.10, 1.71)$ blue; (4.65, 1.60) magenta; and (4.65, 1.71) red. Uupper and lower dot-dashed (cyan) curves correspond to $(\mu_F/m, \mu_R/m) = (4.65, 1.48)$ and (1.25, 1.71), respectively. (b) The uncertainty band on the total charm cross section obtained with the FONLL fiducial parameter set centered around $(m, \mu_F/m, \mu_R/m) = (1.5$ GeV, 1, 1). The central value is given by the solid (red) curve, while the limits of the uncertainty band are shown by the dashed (magenta) curves. The dotted (blue) curve is the result for $(m, \mu_F/m, \mu_R/m) = (1.2$ GeV, 2, 2).

in the region of fixed-target data but is compatible with the scale uncertainties at $\sqrt{s} = 200$ GeV. Because it is based on the energies of the data in the fits, it is not extrapolated to either higher or lower energies.

Lastly, we have added the 2.76 and 7 TeV total cross sections obtained by the ALICE Collaboration in *pp* collisions [24]. These points were not included in our fits. Only the fits where both PHENIX and STAR data are included, giving more weight to the RHIC results, have central cross section values close to the LHC data. While both calculations lie close to the data, the χ^2 for the LHC points is 8.67 with the 2004 STAR point and 3.9 with the latest result.

The individual components of the uncertainty band for the fit including the STAR 2011 data are shown in Fig. 3(a). The uncertainty owing to the charm quark mass (solid curves) dominates for $\sqrt{s} < 100$ GeV, where the scale uncertainty begins to become comparable. Indeed, the scale variations at fixed-target energies are contained within the curves delineating the mass uncertainty. This is very different from the behavior of the fiducial set based on $m = 1.5$ GeV, where the scale variation dominates the uncertainty at all $\sqrt{s}$. As the energy increases, the change in $x \sim 2m/\sqrt{s}$ owing to the mass has a much smaller effect on $xg(x, \mu_F^2)$ than the change in the evolution of the gluon density with μ_F. At higher center-of-mass energies, the curves cluster according to the factorization scale choice. At the top, with the largest growth as a function of $\sqrt{s}$, are the largest values, $\mu_F/m \sim 4.65$. The lowest value of μ_F/m, 1.25, causes the slower growth in cross section because the gluon distribution increases slowly with decreasing x for this value. The uncertainty arising from the range of μ_R/m is rather small, owing to the narrow range of fit values, and shifts the overall magnitude of the curves rather than changing the slope.

The spread in the calculations can be compared to the uncertainty band obtained using the fiducial FONLL parameter set based on $m = 1.5$ GeV [1,4], shown in Fig. 3(b). The prior by-eye fit to the data using $m = 1.2$ GeV, $\mu_F/m = \mu_R/m = 2$ [8] is also shown in this plot. It gives a better representation of the data than the central FONLL parameter set, $m = 1.5$ GeV, $\mu_F/m = \mu_R/m = 1$, and is nearly equivalent to the best χ^2/dof obtained with $m = 1.27$ GeV. It also lies rather close to the LHC points ($\chi^2 = 23.1$), while the central NLO cross section with $m = 1.5$ GeV is a factor of ~3 below these data ($\chi^2 = 142.6$). The upper limit of the uncertainty band in this calculation, obtained with $\mu_R/m = 0.5$, is a factor of ~2 larger than the fitted upper limit because α_s is a factor of ~1.6 larger for $\mu_R = 0.75$ GeV than that calculated for the fit results. On the other hand, the lower limit is a factor of 7–8 below that calculated with the fit results at LHC energies. At collider energies, the slower growth in the cross section with $\sqrt{s}$ is caused by the factorization scale $\mu_F = 0.75$ GeV ($\mu_F/m = 0.5$), below the minimum scale of the PDFs, resulting in backward evolution of the gluon distribution. In the fixed-target energy range, the difference is attributed to the largest mass used, $m = 1.7$ GeV, rather than 1.36 GeV. While the uncertainty band obtained with the FONLL fiducial set is large enough to encompass all possibilities, it is too wide to give the calculation any predictive

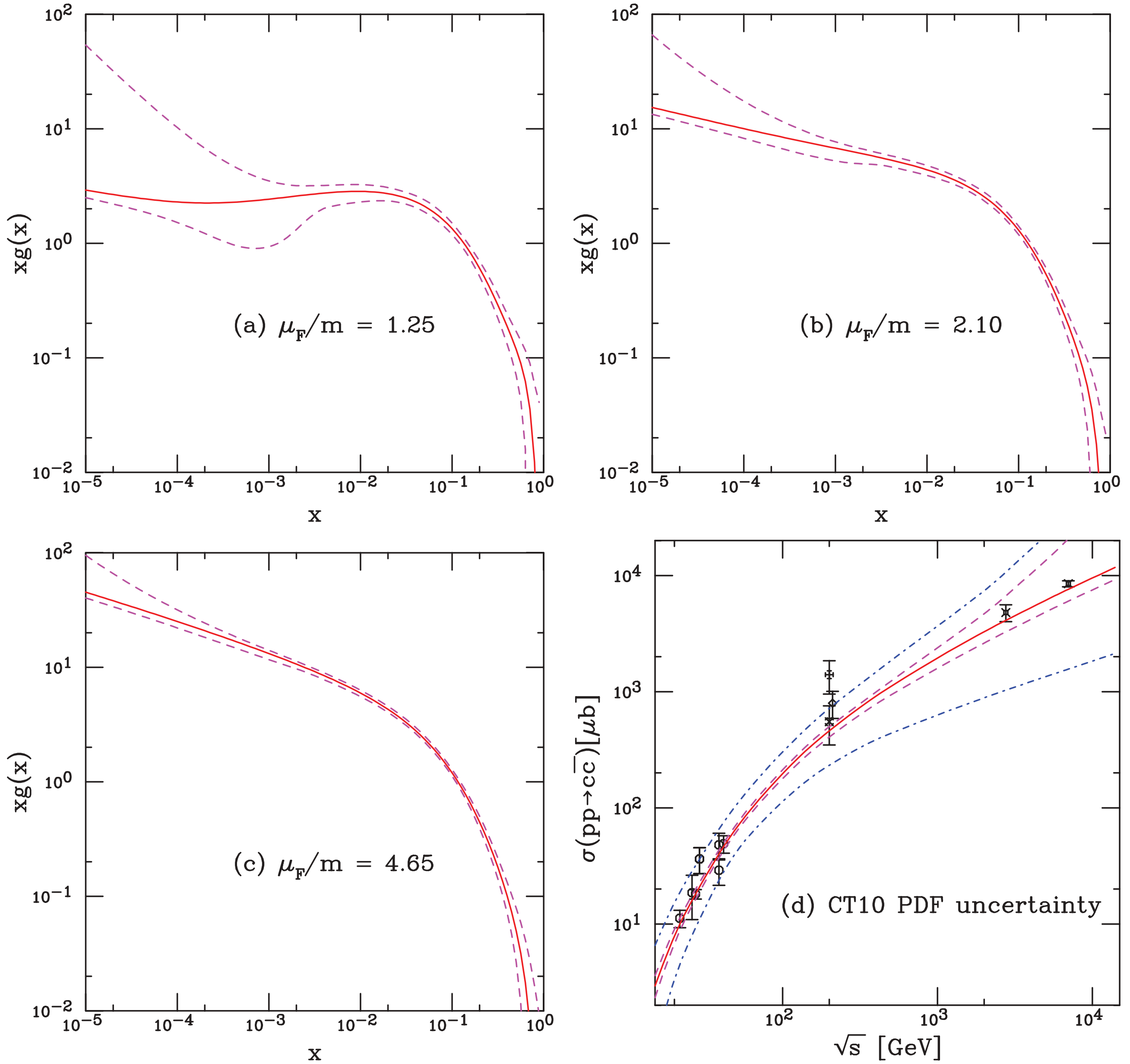

FIG. 4. (Color online) The CT10 gluon distribution, $xg(x, \mu_F)$, is shown for the relevant values of μ_F/m for the total cross section calculation. The central value of the CT10 gluon distribution is given in the solid (red) curve, while the uncertainty band is denoted by the dashed (magenta) curves. The results are shown for (a) the lower limit of μ_F/m, $\mu_F/m = 1.25$; (b) the central value, $\mu_F/m = 2.1$; and (c) the upper limit, $\mu_F/m = 4.65$. (d) The corresponding uncertainty in the total charm cross section owing to the uncertainty in the CT10 gluon distribution is denoted by the dashed (magenta) lines. The total uncertainty owing to the mass and scale uncertainty as well as the gluon uncertainty, combined in quadrature, is given by the dot-dashed (blue) curves.

power. In addition, the scale uncertainty is considerably larger than the mass uncertainty, which should not be true for the physical cross section.

The behavior of the gluon density corresponding to the lower, central, and upper values of μ_F for the fits including the STAR 2011 cross section are shown in Fig. 4. When $\mu_F/m = 1.25$, μ_F is only ~20% higher than μ_0, so that $xg(x, \mu_F^2)$ is almost independent of x for $x < 0.01$. As μ_F/m increases, the growth of the gluon density at low x becomes more pronounced, while the uncertainty band becomes narrower for all values of x. It is clear from these results that the behavior of $xg(x, \mu_F^2)$ determines the growth of the total cross section as a function of the center-of-mass energy.

Because the gluon density is not directly measured, the uncertainty in its behavior as a function of x and μ_F can be important. The largest uncertainty can be expected at low scales. To quantify the uncertainty in the gluon density that enters into our calculations, we also show the resulting uncertainty band obtained by combining all 52 sets for the 26 eigenvectors of the Hessian matrix for the CT10 parton densities. The limits on the behavior of $xg(x, \mu_F^2)$ show the most variation for the lower limit of the factorization scale [see Fig. 4(a)]. There is a sharp increase in the upper limit for $x < 0.001$, while the lower limit on the band has a dip at the same value of x. Using the lower limit of $\mu_F/m = 1.31$ from the latest analysis slightly reduces the variation in the band. As μ_F/m increases, the growth of the gluon density at low x becomes more pronounced, while the uncertainty band becomes narrower for all values of x.

The dashed curves in Fig. 4(d) show the uncertainty in the total charm cross section owing to the variation of the proton parton density. We have used the scale uncertainties from the fit to the 2011 STAR result [22] here. We note that while we have shown the uncertainty bands in the gluon density in Figs. 4(a)–4(c), the cross section uncertainty shown here includes the variations in both the quark and the gluon densities. In general, the uncertainty owing to the parton densities is smaller than that owing to the scale choice. The combined effect of the mass, scale, and parton density uncertainties is given by the dot-dashed curves. It is generally only somewhat wider than that owing to the mass and scale uncertainties alone except for the upper limit of the band at $\sqrt{s} > 1$ TeV.

We now discuss how our results for the mass and scale parameters affect the kinematic distributions of semileptonic decays of charm. The state-of-the-art calculational method for single inclusive heavy-quark production and decay is the FONLL approach [25]. In addition to including the full fixed-order NLO result [5,26], the FONLL calculation also resums [27] large perturbative terms proportional to $\alpha_s^n \log^k(p_T/m)$ to all orders with next-to-leading logarithmic (NLL) accuracy (*i.e.* $k = n,\ n-1$). The total cross sections obtained by integrating the FONLL kinematic distributions, Eq. (4), should be equivalent to that obtained by convoluting the total partonic cross sections with parton densities, Eq. (1), when the same number of light flavors is employed.

The main difference in the two approaches that might affect the total charm cross section is the number of active flavors. In the FONLL approach, the heavy quark is treated as an active light flavor at $p_T \gg m$. Thus the number of light flavors used to calculate α_s includes the heavy quark, i.e., $n_{\rm lf} + 1$, where, for charm, $n_{\rm lf} = 3$ (u, d, and s). The same number of flavors, $n_{\rm lf} + 1$, is also used in the fixed-order component of the FONLL calculation for self-consistency. Therefore, a total charm cross section calculated in the FONLL approach will automatically be lower than the result with the same mass and scale parameters in Eq. (1) with $n_{\rm lf} = 3$, as $\alpha_s(n_{\rm lf} = 4) < \alpha_s(n_{\rm lf} = 3)$. When the renormalization scale is of the order of the quark mass, the difference in the total cross sections at $\sqrt{s} = 200$ GeV is less than 20% [4]. However, for $\mu_R/m < 1$, $\alpha_s(\mu_R)$ grows faster with decreasing μ_R so that the upper limit on the NLO cross section is up to a factor of two larger than that obtained with FONLL. On the other hand, the lower limit, obtained with $\mu_R/m = 2$, is very similar in the two calculations. Thus whether charm is treated as a heavy ($n_{\rm lf}$) or an active ($n_{\rm lf} + 1$) flavor in the calculation turns out to be one of the most important influences on the limits of the charm uncertainty comparing the NLO and FONLL results. When the total charm cross section is calculated with $n_{\rm lf}$ in the FONLL approach, i.e., the charm quark is treated as a heavy rather than an active flavor, the results are in agreement with the NLO calculations [28].

The calculation of the inclusive electron spectrum from heavy-flavor decay involves three components: the p_T and rapidity distributions of the heavy quark Q, calculated in perturbative QCD; fragmentation of the heavy quarks into heavy hadrons, H_Q, described by phenomenological input extracted from e^+e^- data; and the decay of H_Q into electrons according to spectra available from other measurements, schematically written as [2]

$$\frac{Ed^3\sigma(e)}{dp^3} = \frac{E_Q d^3\sigma(Q)}{dp_Q^3} \otimes D(Q \to H_Q) \otimes f(H_Q \to e) \tag{4}$$

where the symbol $\otimes$ denotes a generic convolution. The fragmentation of quarks into hadrons is denoted $D(Q \to H_Q)$. The electron decay spectrum, $f(H_Q \to e)$, accounts for the semileptonic branching ratios.

Figure 5 shows the lepton spectra arising from semileptonic heavy-flavor decays at $\sqrt{s} = 200$ GeV, all calculated in the FONLL approach. The $B \to e$ and $B \to D \to e$ bands, as well as the red $D \to e$ band, are calculated with the same fiducial set of parameters as in Ref. [2]. The dashed (black) curves represent the $D \to e$ band calculated for our best-fit parameter set, including both the PHENIX and the 2011 STAR total cross sections. The new $D \to e$ calculation is much narrower. It lies completely within the uncertainty band based on the fiducial parameter set with the central value of the charm quark mass fixed at $m = 1.5$ GeV. At low p_T, $p_T < 2.5$ GeV, the new $D \to e$ band is near the top of the fiducial FONLL $D \to e$ band, while for $p_T \geqslant 7.5$ GeV, the new set gives a result near the bottom of the fiducial $D \to e$ band. The transition from dominance of the electron spectra by charm decays to dominance by bottom decays happens at a lower p_T with the $m = 1.27$ GeV set.

The right-hand side of Fig. 5 shows the sum of the $D \to e$, $B \to e$, and $B \to D \to e$ for the two cases. The PHENIX nonphotonic electron data are compatible with the top of the sum of the uncertainty bands with the fiducial FONLL set. However, the data now lie somewhat above the band obtained when the best-fit $D \to e$ contribution to charm production replaces the fiducial contribution. The agreement with the data is worst at intermediate values of p_T, $p_T \sim 5$ GeV, where the c and b contributions to the electron spectra are nearly equal. This discrepancy is not so surprising because the best-fit parameters were obtained using the NLO QCD calculation with $n_{\rm lf} = 3$ flavors, while the FONLL calculation, both in the fixed-flavor scheme and in the full FONLL result, uses $n_{\rm lf} + 1 = 4$, as the heavy quark is treated as an active light flavor over all p_T. The value of $\alpha_s(\mu_R^2)$ obtained with four light flavors is smaller than that obtained with three light flavors, even for the same value of μ_R. More importantly, the range of factorization scales is larger for our best-fit case, $1.59 < \mu_F < 5.9$ GeV ($1.25 \leqslant \mu_F/m \leqslant 4.65$), instead of $0.75 < \mu_F < 3$ GeV ($0.5 \leqslant \mu_F/m \leqslant 2$) for the fiducial set. The higher factorization scales cause the p_T distribution to fall

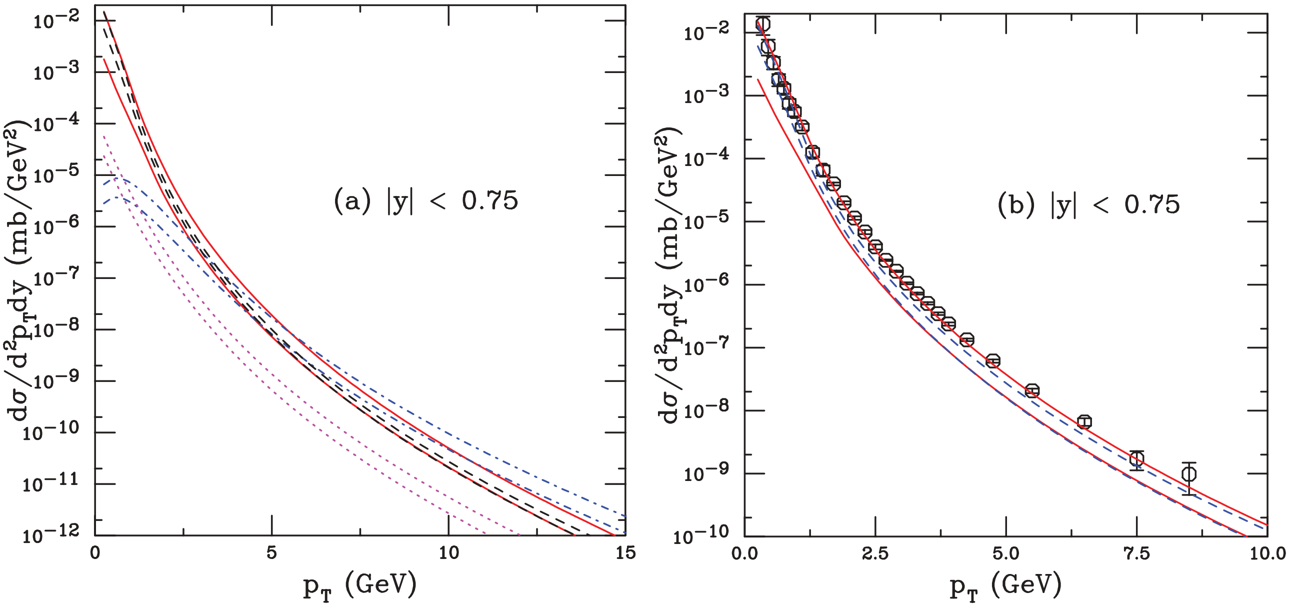

FIG. 5. (Color online) (a) Components of the nonphotonic electron spectrum: $B \to e$ [dot-dashed (blue) line]; $B \to D \to e$ [dotted (magenta) line]; $D \to e$ both with the FONLL parameters [solid (red) line] and with those for $m = 1.27$ GeV in Fig. 1(d) [dashed (black) line] at $|y| < 0.75$ in $\sqrt{s} = 200$ GeV pp collisions. (b) The sum of the contributions is compared with the FONLL set for charm [solid (red) line] and that with $m = 1.27$ GeV [dashed (blue) line]. The PHENIX data [20] are also shown.

off faster with p_T in the best-fit case. The difference is apparent already in the charm quark p_T distributions and would be enhanced for the semileptonic charm decays to electrons, as the decay leptons carry only ~30% of the parent hadron p_T [29].

Figure 6 compares our calculations with the ALICE single-muon data in the forward rapidity region, $2.5 < y < 4$ [30]. The data are given for $2 < p_T < 12$ GeV, both over the full rapidity region [Fig. 6(a)] and separated into five rapidity bins, each 0.3 unit wide [Fig. 6(b)]. The calculations with both the fiducial charm parameter set[1] (solid line) and our charm fit (dashed line) are compared to the data in Fig. 6(a). The two bands are indistinguishable for $p_T > 5$ GeV. Therefore, for clarity, we compare the muon p_T distributions in the narrow rapidity bins to only our calculations with the mass and scale parameters from the charm fit. The calculations agree well with the measurements over the entire p_T range.

In Figs. 6(c) and 6(d) we present the results as a function of rapidity integrated over the same p_T range as the data, $2 < p_T < 12$ GeV. Figure 6(c) shows the upper and lower limits of the FONLL calculations of $B \to \mu$ and $B \to D \to \mu$ in the dot-dashed (blue) and dotted (magenta) curves, respectively. The FONLL $D \to \mu$ uncertainty bands with the fiducial charm parameter set are shown by the solid curves, while the dashed curves are calculated with the charm fit parameters. The sums of the heavy-flavor decay contributions to the rapidity distribution are compared on a linear scale in Fig. 6(d). The p_T-integrated ALICE data agree well with both calculations. The results with the fitted charm parameter set narrow the uncertainty band without sacrificing the consistency with the measured data.

While the agreement between the lepton measurements at RHIC and LHC and our calculations is encouraging, as noted here and in Ref. [2], there is significant admixture of semileptonic charm and bottom decays, particularly at lepton $p_T > 4$ GeV. A better test of our results would be a comparison to open charm hadron data. Thus, in Figs. 7 and 8, we show the D^0 [Figs. 7(a) and 8(a)], D^+ [Figs. 7(b) and 8(b)], and D^{*+} [Figs. 7(c) and 8(c)] distributions in the ALICE [32] and the LHCb [33] acceptances at midrapidity and forward rapidity, respectively.

Figure 7 compares the FONLL calculations with the fiducial parameter set [solid (red) lines] with the fitted parameters based on $m = 1.27$ GeV [dashed (blue) lines]. The upper and lower limits of both bands are shown. While the ALICE data are in agreement with the upper limits of both calculations, the large D meson uncertainty is reduced at low p_T with the fitted parameter set.

Figure 8 shows the upper and lower limits of the FONLL calculation based on $m = 1.27$ GeV in the five rapidity intervals of $\Delta y = 0.5$ in the range $2 < y < 4.5$ covered by the LHCb detector. In most cases here also the agreement with the data is very good, the exception being the most forward rapidity measurement of D^{*+}, where the calculation is above the data. Interestingly, while the normalizations of the D^* and D^+ calculations are rather similar over all of the rapidity intervals [compare Figs. 8(b) and 8(c)], there is a significant drop in the measured D^* cross section at low p_T between $3.5 < y < 4$ and $4 < y < 4.5$ that is not reproduced in the calculations.

---

[1] For a complete discussion of LHC predictions using the fiducial FONLL parameter set, see Ref. [31].

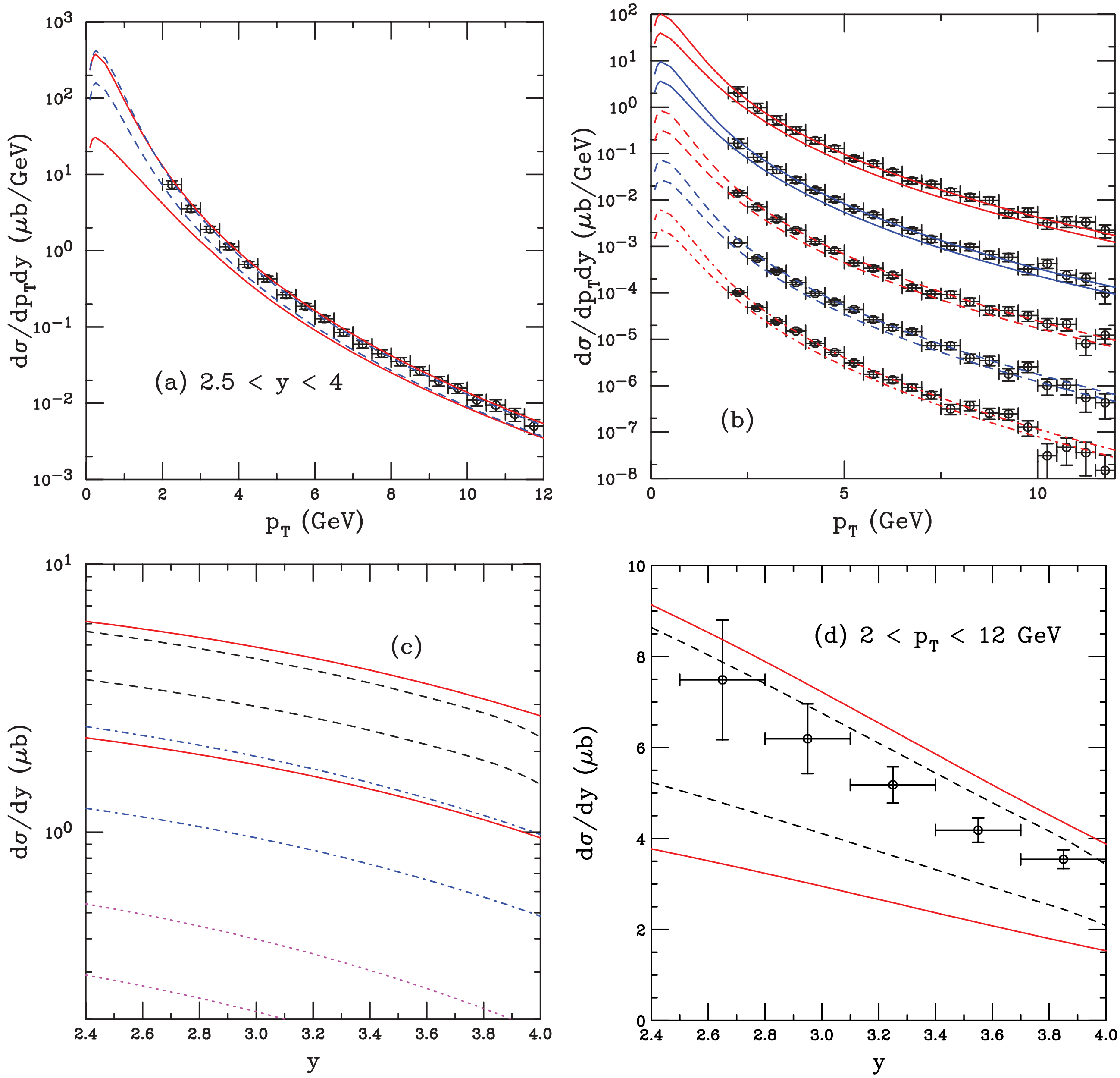

FIG. 6. (Color online) Our calculations are compared with the ALICE inclusive single-muon data from heavy-flavor decays [30] at $\sqrt{s} = 7$ TeV. (a) Comparison of the single-lepton p_T distributions in the rapidity interval $2.5 < y < 4$ at $\sqrt{s} = 7$ TeV calculated with the FONLL set for charm [solid (red) line] and the fitted set with $m = 1.27$ GeV [dashed (black) line]. (b) Contributions to the p_T distributions in (a) divided into rapidity bins, from top to bottom: $2.5 < y < 2.8$ [solid (red) line]; $2.8 < y < 3.1$ [solid (blue) line]; $3.1 < y < 3.4$ [dashed (red) line]; $3.4 < y < 3.7$ [dashed (blue) line]; and $3.7 < y < 4$ [dot-dashed (red) line]. The top curves are shown at their calculated value; the others are scaled down by successive factors of 10, to separate them. (c) Components of the rapidity distribution at $\sqrt{s} = 7$ TeV with $2 \leqslant p_T \leqslant 12$ GeV, $B \to \mu$ [dot-dashed (blue) line]; $B \to D \to \mu$ [dotted (magenta) line]; $D \to \mu$ both with the FONLL parameters [solid (red) line] and with those for $m = 1.27$ GeV in Fig. 1(d) [dashed (black) line]. (d) The sums of the contributions are compared with the FONLL set for charm [solid (red) line] and that with $m = 1.27$ GeV [dashed (black) line].

We have shown that the calculated uncertainties in the total charm cross section can be considerably reduced by fitting the data with an NLO calculation. When the same fit parameters are used to calculate the leptons from heavy-flavor decays in the FONLL approach, the results are still in agreement with the data.

III. QUARKONIUM PRODUCTION IN THE COLOR EVAPORATION MODEL

We now turn to a treatment of quarkonium production within this same framework. Perhaps the simplest approach to quarkonium production is the CEM, which treats heavy flavor

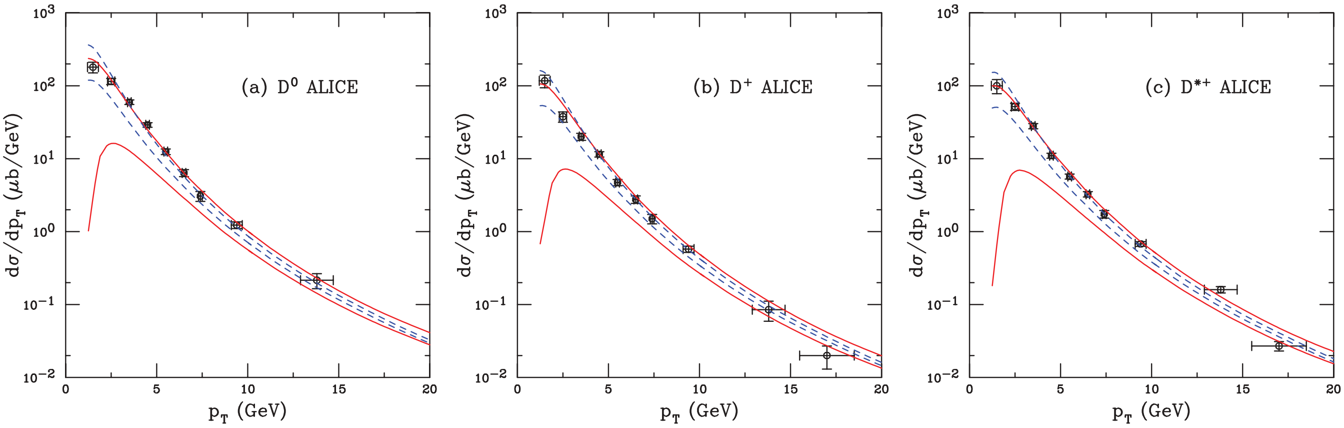

FIG. 7. (Color online) Our calculations are compared with the reconstructed ALICE (a) D^0, (b) D^+, and (c) D^{*+} meson data [32] at $\sqrt{s} = 7$ TeV in $|y| \leqslant 0.5$. The FONLL uncertainty bands with the fiducial charm parameter set are shown by the solid (red) curves, while the dashed (blue) curves are calculated with the charm fit parameters.

and quarkonium production on an equal footing. The CEM was first discussed some time ago [34,35] and has enjoyed considerable phenomenological success when applied at NLO in the total cross section and leading order in the quarkonium p_T distribution [3,36,37].

In the CEM, the quarkonium production cross section is some fraction, F_C, of all $Q\overline{Q}$ pairs below the $H\overline{H}$ threshold, where H is the lowest mass heavy-flavor hadron. Thus the CEM cross section is simply the $Q\overline{Q}$ production cross section with a cut in the pair mass but without any constraints on the color or spin of the final state. The color of the octet $Q\overline{Q}$ state is "evaporated" through an unspecified process which does not change the momentum. The additional energy needed to produce heavy-flavored hadrons when the partonic center-of-mass energy, $\sqrt{\hat{s}}$, is less than $2m_H$, the $H\overline{H}$ threshold energy, is nonperturbatively obtained from the color field in the interaction region. Thus the quarkonium yield may be only a small fraction of the total $Q\overline{Q}$ cross section below $2m_H$. At leading order, the production cross section of quarkonium state C in a pp collision is

$$\sigma_C^{\rm CEM}(s_{_{NN}}) = F_C \sum_{i,j} \int_{4m^2}^{4m_H^2} ds \int dx_1\, dx_2\, f_i^p(x_1, \mu_F^2) \times f_j^p(x_2, \mu_F^2)\hat{\sigma}_{ij}(\hat{s}, \mu_F^2, \mu_R^2), \quad (5)$$

where $ij = q\overline{q}$ or gg and $\hat{\sigma}_{ij}(\hat{s})$ is the $ij \to Q\overline{Q}$ subprocess cross section.

The fraction F_C must be universal so that, once it is fixed by data, the quarkonium production ratios should be constant as a function of $\sqrt{s}$, y, and p_T. The actual value of F_C depends on the heavy-quark mass, m, the scale parameters, the parton densities, and the order of the calculation. It was shown in Ref. [3] that the quarkonium production ratios were indeed relatively constant, as expected by the model. In addition,

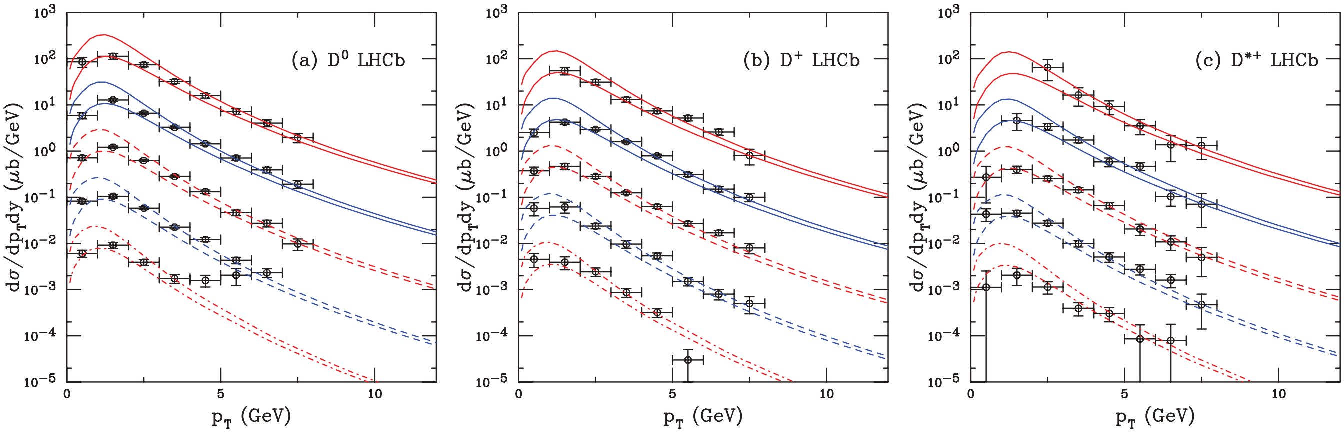

FIG. 8. (Color online) Our calculations are compared with the reconstructed LHCb (a) D^0, (b) D^+, and (c) D^{*+} meson data [33] at $\sqrt{s} = 7$ TeV in the rapidity intervals $2 < y < 2.5$ [solid (red) line]; $2.5 < y < 3$ [solid (blue) line]; $3 < y < 3.5$ [dashed (red) line]; $3.5 < y < 4$ [dashed (blue) line]; and $4 < y < 4.5$ [dot-dashed (red) line]. The curves are calculated with the charm fit parameters. The sets of results are separated by a factor of 10 between rapidity intervals to facilitate comparison. The lowest rapidity interval, $2 < y < 2.5$, is not scaled.

Ref. [36] showed that the data on the J/ψ and open charm cross sections as a function of $\sqrt{s}$ in hadroproduction and $W_{\gamma N}$ in photoproduction have the same energy dependence.

The data we use to obtain F_C for the J/ψ are from the compilation by Maltoni *et al.* [38]. The data range from fixed-target experiments with center-of-mass energy $6.8 \leqslant \sqrt{s} \leqslant 41.6$ GeV [39–56] to data from the CERN ISR at $\sqrt{s} = 23$ GeV [57], 30 GeV [58], 30.6 GeV [59], 31 GeV [57], 52 GeV [60,61], 52.4 GeV [59], 53 GeV [57,58], 62.7 GeV [59], and 63 GeV [57,58]. Data from the PHENIX experiment at RHIC [62] are also used. The ISR data [57–61] are all from pp measurements, as are the data from Refs. [40,43]. Data from single nuclear targets include Be [41,42,48,53], Li [46], C [44,45], Si [54], Fe [49], Au [55], and Pt [43]. Other experiments took data on multiple nuclear targets [39,50–52,56]. Both the total forward cross section ($x_F > 0$) [39–56,62] and the cross section times the branching ratio to lepton pairs, B_{ll}, at $y = 0$, $B_{ll} d\sigma/dy|_{y=0}$ [41,42,47–52,54–62], were reported. Several of the ISR experiments [57–59,61] only provided the cross section at $y = 0$, likely owing to their limited phase-space coverage. In cases where the total cross section was reported, the uncertainty provided was on the level of 40%. We note that several detectors have taken data at the same energy and with the same target but reported results with different experiment numbers that diverge by more than $1\sigma_\chi$. For example, the p + C results reported by E331 [44] and E444 [45] using the same apparatus, $\sigma = 256 \pm 30$ and 166 ± 23 nb/nucleon, respectively, differ by more than $2\sigma_\chi$.

Maltoni and collaborators corrected prior measurements using up-to-date values of the J/ψ branching ratios to $\mu^+\mu^-$ and e^+e^- [63] and, when appropriate, averaged the results on multiple nuclear targets assuming $\sigma_{pA}/\sigma_{pp} = A^\alpha$ with $\alpha = 0.96 \pm 0.01$ [64] at $x_F \sim 0$, obtained with an 800-GeV proton beam [38]. The A dependence was assumed to be independent of the center-of-mass energy. However, a recent reanalysis of these data, assuming a combination of shadowing and absorption effects on J/ψ production, found that, at $x_F \sim 0$, the absorption cross section decreases as a function of the incident energy whether or not the data were corrected for shadowing effects [65]. Later measurements with $p_{\rm lab} = 158$ GeV obtained an absorption cross section consistent with the predicted extrapolation [66]. In addition, effects arising from modifications of the parton densities in the nucleus that may be present in the data depend on the magnitude of A and have not been taken into account in the averaging. Thus the effective α, which includes all relevant nuclear effects, likely depends on the incident energy.

We have fit F_C both to the full data set and to more limited sets. Our final result is based on the total cross section data with only p, Be, Li, C, and Si targets, respectively. In this way, we avoid uncertainties owing to ignoring any cold nuclear matter effects, which are of the order of a few percent in light targets. We also restricted ourselves to forward cross sections only, rather than including the $B_{ll} d\sigma/dy|_{y=0}$ data in the fits. The rapidity distributions calculated in the Mangano-Nason-Ridolfi (MNR) code are subject to fluctuations about the mean, even with high statistics calculations. The total cross sections, not subject to these fluctuations, are thus more accurate.

Our calculations use the NLO $Q\overline{Q}$ code of MNR [67] with the $2m_H$ mass cut in Eq. (5), as described in Refs. [3,68]. Because the NLO $Q\overline{Q}$ code is an exclusive calculation, we take the mass cut on the invariant average over kinematic variables of the c and $\overline{c}$. Thus, instead of defining μ_F and μ_R relative to the quark mass, they are defined relative to the transverse mass, $\mu_{F,R} \propto m_T = \sqrt{m^2 + p_T^2}$, where p_T is that of the $Q\overline{Q}$ pair, $p_T^2 = 0.5(p_{T_Q}^2 + p_{T_{\overline{Q}}}^2)$.

We use the same values of the central charm quark mass and scale parameters as in the previous section, both for the fiducial parameter sets and for the best-fit values, to obtain the normalization F_C. We fit F_C to the J/ψ data for both the fiducial FONLL sets [central value $(m, \mu_F/m, \mu_R/m) = (1.5\,\text{GeV}, 1, 1)$] and the fit results obtained in the previous section [central value $(m, \mu_F/m, \mu_R/m) = (1.27\,\text{GeV}, 2.1, 1.6)$]. We determine F_C only for the central parameter set in each case and scale all the other calculations for that case by the same value of F_C to obtain the extent of the J/ψ uncertainty band employing Eqs. (2) and (3).

We find $F_C = 0.040377$ for the central result, $(m, \mu_F/m, \mu_R/m) = (1.5\text{ GeV}, 1, 1)$, and $F_C = 0.020393$ for the central CT10 result with $(m, \mu_F/m, \mu_R/m) = (1.27\text{ GeV}, 2.1, 1.6)$. A significantly larger value of F_C is necessary for the larger quark mass, as the fraction of the total charm cross section remaining after the mass cut is smaller. The results for the energy dependence of the forward inclusive J/ψ cross section are shown in Figs. 9 and 10 for the central mass values of 1.5 and 1.27 GeV, respectively. The uncertainty bands are shown on the left in these figures, while the individual parameter sets contributing to the bands are shown on the right.

The most obvious result in Fig. 9(a) is that there is no well-defined lower limit on the total cross section with the fiducial parameter set, only an upper limit. The reason is apparent from Fig. 9(b): the combined differences in the minimum values of the masses and scales added in quadrature are larger than the central value for $\sqrt{s} < 63$ GeV. When the fiducial parameter sets are applied to the CEM calculation of J/ψ production, the upper limit of the charm quark mass, $m = 1.7$ GeV, gives a very narrow invariant mass interval for the CEM calculation in Eq. (5), from $2m = 3.4$ GeV to $2m_D = 3.86$ GeV. The difference between the results with different quark masses is more pronounced at low center-of-mass energies, while the energy dependence of the calculations with different values of m begins to converge at large $\sqrt{s}$. Indeed, the "hump" in the upper limit of the fiducial uncertainty band is caused by the slower growth of $(m, \mu_F/m_T, \mu_R/m_T) = (1.3\text{ GeV}, 1, 1)$ relative to $(1.5\text{ GeV}, 1, 0.5)$ for $\sqrt{s} > 400$ GeV; note the crossing of the solid and dashed blue curves in Fig. 9(b). We also note that the fiducial set does not give very good agreement with the total J/ψ cross section reported by CDF [69], as the calculated $\sqrt{s}$ dependence is too slow to match the measured growth of the forward cross section.

The best-fit band, shown in Fig. 10(a), on the other hand, gives very good agreement with the J/ψ data over the entire energy range, even for the CDF cross section, not included in the fit. The data are almost all encompassed by the width of the band. Now, as was the case for the total charm cross section,

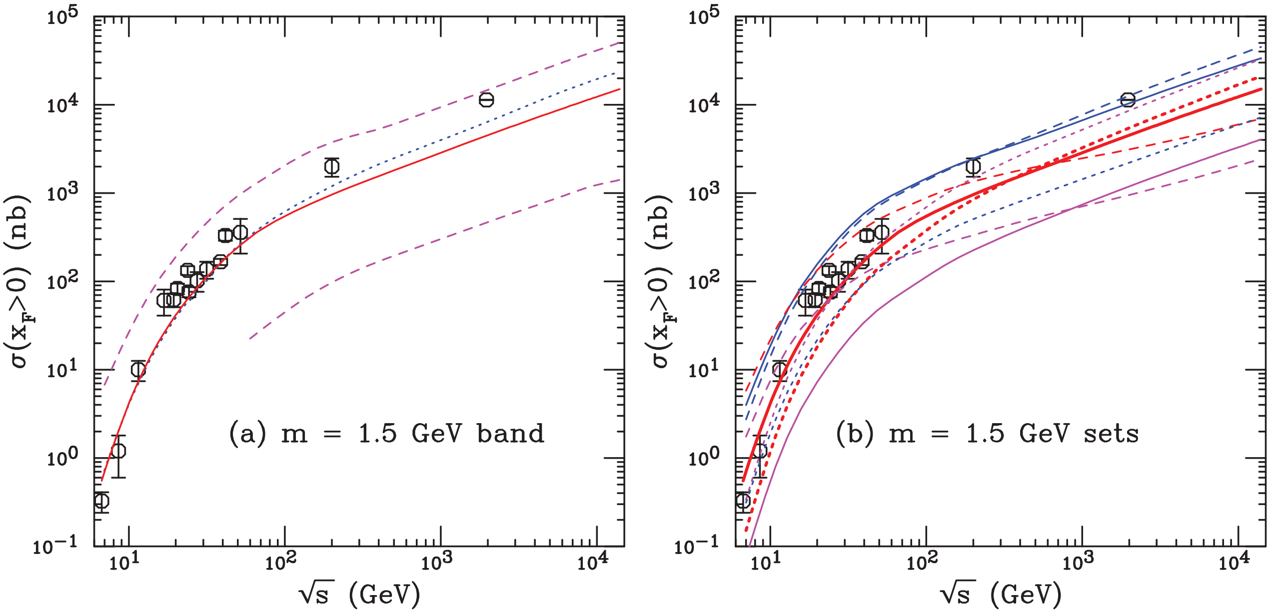

FIG. 9. (Color online) Forward J/ψ cross sections calculated with the FONLL fiducial parameter set with $m = 1.5$ GeV. (a) The uncertainty band obtained employing the FONLL parameter set. The solid (red) curve is the central value, while the limits of the uncertainty band are shown by the dashed (magenta) curves. The dotted (blue) curve is a result with $(m, \mu_F/m_T, \mu_R/m_T) = (1.2\text{ GeV}, 2, 2)$. (b) The solid (red) curve is the central value $(m, \mu_F/m_T, \mu_R/m_T) = (1.5\text{ GeV}, 1, 1)$. The solid blue and magenta curves outline the mass uncertainty with (1.3 GeV, 1, 1) and (1.7 GeV, 1, 1) respectively. Dashed curves are associated with $\mu/m_T = 0.5$: $(\mu_F/m_T, \mu_R/m_T) = (1, 0.5)$ blue, (0.5,1) magenta, and (0.5,0.5) red. Dotted curves are associated with $\mu/m_T = 2$: $(\mu_F/m_T, \mu_R/m_T) = (1, 2)$ blue, (2,1) magenta, and (2,2) red.

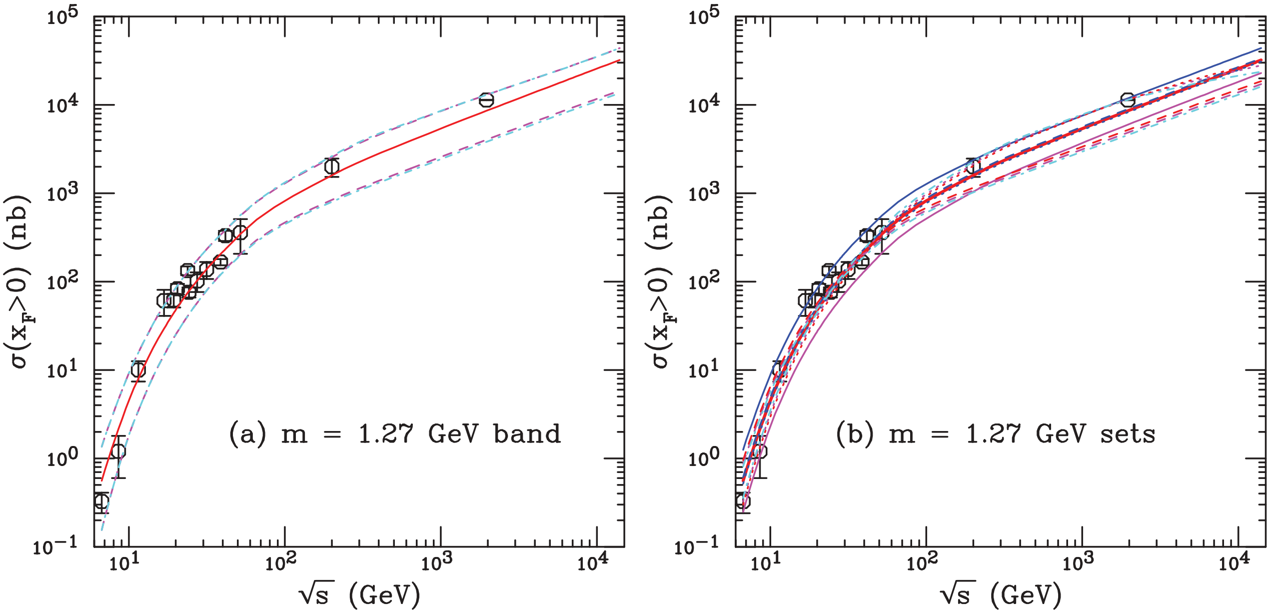

FIG. 10. (Color online) (a) The uncertainty band on the forward J/ψ cross section calculated based on the $c\overline{c}$ parameter fit in Fig. 2(d). The dashed (magenta) curves and dot-dashed (cyan) curves show the extent of the corresponding uncertainty bands. Dashed curves outline the most extreme limits of the band. (b) Components of the uncertainty band. The central value $(m, \mu_F/m_T, \mu_R/m_T) = (1.27\text{ GeV}, 2.10, 1.60)$ is given by the solid red curve. The solid blue and magenta curves outline the mass uncertainty with (1.18 GeV, 2.10, 1.60) and (1.36 GeV, 2.10, 1.60), respectively. Dashed curves outline the lower limits on the scale uncertainty: $(\mu_F/m_T, \mu_R/m_T) = (2.10, 1.48)$ blue; (1.25, 1.60) magenta; and (1.25, 1.48) red. Dotted curves outline the upper limits on the scale uncertainty: $(\mu_F/m_T, \mu_R/m_T) = (2.10, 1.71)$ blue; (4.65, 1.60) magenta; and (4.65, 1.71) red. The upper and lower dot-dashed (cyan) curves correspond to $(\mu_F/m_T, \mu_R/m_T) = (4.65, 1.48)$ and (1.25, 1.71), respectively.

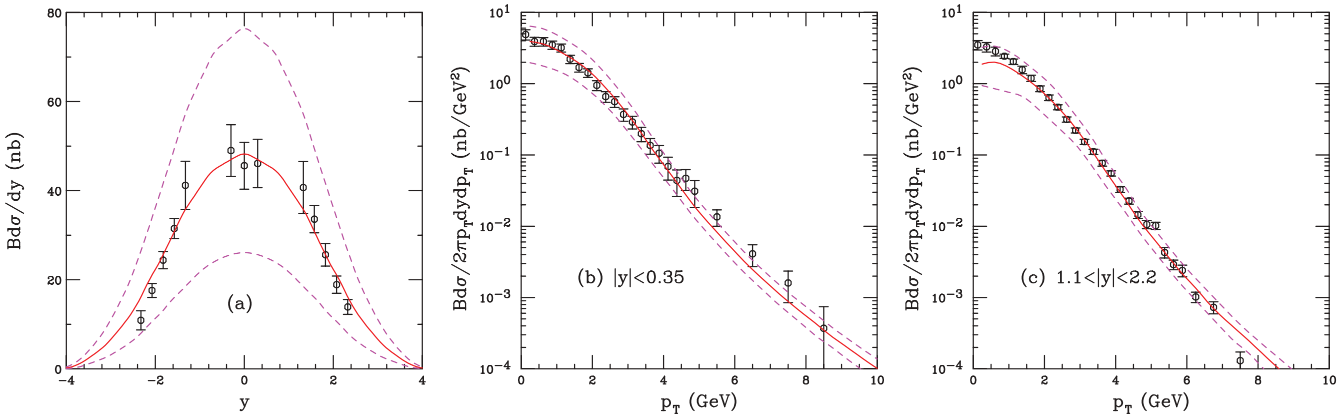

FIG. 11. (Color online) The J/ψ rapidity distribution (a) and the midrapidity (b) and forward rapidity (c) p_T distributions and their uncertainties calculated with the same parameters as in Fig. 1(d). The results are compared to PHENIX pp measurements at $\sqrt{s} = 200$ GeV [70]. The correlated and uncorrelated systematic errors in Ref. [70] are added in quadrature. No additional scaling factor has been applied. The solid (red) curve shows the central value, while the dashed (magenta) curves outline the uncertainty band. A $\langle k_T^2 \rangle_p$ kick of 1.19 GeV^2 is applied to the p_T distributions, as discussed in the text.

the uncertainty owing to the quark mass dominates over that owing to the scale choice for $\sqrt{s} < 200$ GeV.

We now turn to the J/ψ rapidity and p_T distributions, shown in Fig. 11 for $\sqrt{s} = 200$ GeV, Fig. 12 for $\sqrt{s} = 7$ TeV and Fig. 13 for $\sqrt{s} = 2.76$ TeV. At leading order in the total cross section, the $Q\overline{Q}$ pair p_T is 0. Thus, while our calculation is NLO in the total cross section, it is leading order in the quarkonium p_T distributions. In the exclusive NLO calculation [67] both the Q and the $\overline{Q}$ variables are integrated to obtain the pair distributions; recall that $\mu_{F,R} \propto m_T$.

Results on open heavy flavors indicate that some level of transverse momentum broadening is needed to obtain agreement with the low-p_T data. This is often done by including some intrinsic transverse momentum, k_T, smearing to the initial-state parton densities. The implementation of intrinsic k_T in the MNR code is not handled in the same way as calculations of other hard processes owing to the nature of the code. In the MNR code, the cancellation of divergences is done numerically. Because adding additional numerical Monte Carlo integrations would slow the simulation of events, in addition to requiring multiple runs with the same setup but different intrinsic k_T kicks, the kick is added in the final, rather than the initial, state. In Eq. (5), the Gaussian function $g_p(k_T)$,

$$g_p(k_T) = \frac{1}{\pi \langle k_T^2 \rangle_p} \exp\left(-k_T^2 / \langle k_T^2 \rangle_p\right) \tag{6}$$

[71], multiplies the parton distribution functions for both hadrons, assuming that the x and k_T dependencies in the initial partons completely factorize. If factorization applies, it does not matter whether the k_T dependence appears in the initial or final state if the kick is not too large, as described below. In Ref. [71], $\langle k_T^2 \rangle_p = 1$ GeV^2 was found to best describe fixed-target charm production.

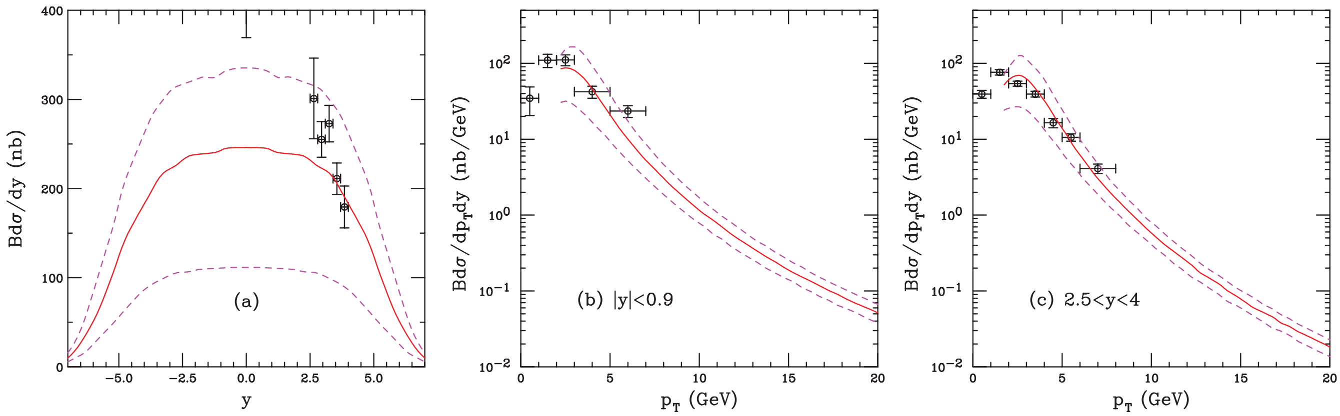

FIG. 12. (Color online) The J/ψ rapidity distribution (a) and the midrapidity, $|y| < 0.9$ (b), and forward rapidity, $2.5 < y < 4$ (c), p_T distributions at $\sqrt{s} = 7$ TeV and their uncertainties calculated with the same parameters as in Fig. 1(d). The results are compared to the ALICE rapidity distribution as well as the mid- and forward rapidity p_T distributions [72]. No additional scaling factor has been applied. The solid (red) curve shows the central value, while the dashed (magenta) curves outline the uncertainty band. A $\langle k_T^2 \rangle_p$ kick of 1.49 GeV^2 is applied to the p_T distributions, as discussed in the text.

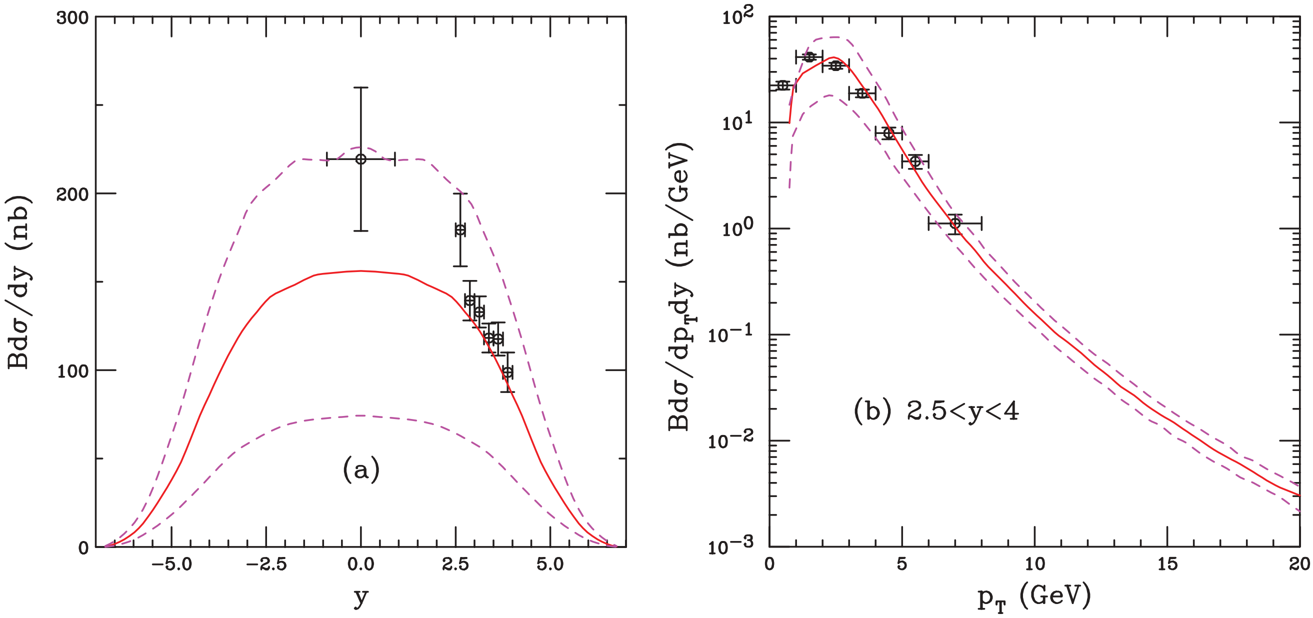

FIG. 13. (Color online) The J/ψ rapidity distribution (a) and the forward rapidity, $2.5 < y < 4$ p_T, distribution (b) at $\sqrt{s} = 2.76$ TeV and their uncertainties calculated with the same parameters as in Fig. 1(d). The results are compared to the ALICE rapidity distribution as well as the forward rapidity p_T distribution [73]. No additional scaling factor has been applied. The solid (red) curve shows the central value, while the dashed (magenta) curves outline the uncertainty band. A $\langle k_T^2\rangle_p$ kick of 1.41 GeV^2 is applied to the p_T distributions, as discussed in the text.

In the code, the $Q\overline{Q}$ system is boosted to rest from its longitudinal center-of-mass frame. Intrinsic transverse momenta of the incoming partons, $\vec{k}_{T1}$ and $\vec{k}_{T2}$, are chosen at random with k_{T1}^2 and k_{T2}^2 distributed according to Eq. (6). A second transverse boost out of the pair rest frame changes the initial transverse momentum of the $Q\overline{Q}$ pair, $\vec{p}_T$, to $\vec{p}_T + \vec{k}_{T1} + \vec{k}_{T2}$. The initial k_T of the partons could have alternatively been given to the entire final-state system, as is essentially done if applied in the initial state, instead of to the $Q\overline{Q}$ pair. There is no difference if the calculation is leading order only but at NLO an additional light parton can also appear in the final state so the correspondence is not exact. In Ref. [71], the difference between the two implementations is claimed to be small if $k_T^2 \leqslant 2\,\mathrm{GeV}^2$. We note that the rapidity distribution, integrated over all p_T, is unaffected by the intrinsic k_T.

The effect of the intrinsic k_T on the shape of the J/ψ p_T distribution can be expected to decrease as $\sqrt{s}$ increases because the average p_T of the J/ψ also increases with energy. However, the value of $\langle k_T^2\rangle_p$ may increase with $\sqrt{s}$. We can check the energy dependence of $\langle k_T^2\rangle_p$ by the shape of the J/ψ p_T distributions at central and forward rapidity at RHIC. We find that $\langle k_T^2\rangle_p = 1 + (1/12)\ln(\sqrt{s}/20) \approx 1.19$ GeV^2 at $\sqrt{s} = 200$ GeV agrees well with the J/ψ p_T distributions measured by PHENIX at both midrapidity and forward rapidity (see Fig. 11). The rapidity distributions, as well as the p_T distributions in the two rapidity regions, all agree well with the J/ψ cross sections calculated with the central set of parameters. Only the low-p_T part of the forward rapidity p_T distribution is somewhat underestimated. The integrated forward cross section is about 50% lower than the midrapidity value. In addition, the p_T distribution falls off faster at high p_T in the forward rapidity region.

The ALICE 7 TeV p_T distributions, shown in Figs. 12(b) and 12(c), include the ALICE rapidity cuts for the central and forward rapidity regions, $|y| < 0.9$ and $2.5 < y < 4$, respectively. The rapidity distribution at $\sqrt{s} = 7$ TeV [Fig. 12(a)] is flat over several units of rapidity. Thus the integrated cross sections in the two rapidity intervals, normalized per unit of rapidity, are very similar. However, the forward rapidity p_T distribution is still a stronger function of p_T than the midrapidity distribution.

Finally, the inclusive J/ψ rapidity distribution and forward rapidity p_T distribution at $\sqrt{s} = 2.76$ TeV are compared to the ALICE data in Fig. 13. There the calculated rapidity distribution is not as broad and the agreement with the data is rather good, although the midrapidity point remains high relative to the central value of the calculation. The agreement of the calculated p_T distribution with the forward rapidity data is quite good with the exception of the lowest p_T point, where the calculated distribution turns over more quickly than the data.

IV. SUMMARY

We have narrowed the uncertainty band on the open heavy-flavor cross section and, in so doing, have also provided a realistic uncertainty band on J/ψ production in the CEM. The central result, $m = 1.27$ GeV, $\mu_F/m = 2.1$, and $\mu_R/m = 1.6$, is quite compatible with previous calculations using a "by-eye" fit to the data with $m = 1.2$ GeV, $\mu_F/m = \mu_R/m = 2$ [3,8].

While the fits have been made by comparing the calculated NLO charm production cross section to available data at fixed-target energies and at RHIC, they are in good agreement with the extracted total charm cross sections at the LHC. The same parameter set also provides good agreement with the distributions of single leptons from semileptonic heavy-flavor decays at RHIC and the LHC. The limit on the width of the uncertainty band is now set by the uncertainty owing to bottom quark production and decay.

We have used the same fit parameters in the calculation of J/ψ production in the CEM and have thus provided the first uncertainty band on J/ψ production in this approach. The energy dependence of the total J/ψ cross section that results is a good match to the data up to collider energies. The p_T distributions are also in good agreement with the data from RHIC and the LHC. In future work, we will use our new parameter set to place limits on the contribution of B meson decays to J/ψ production and will also study cold nuclear matter effects on J/ψ production.

ACKNOWLEDGMENTS

We thank M. Cheng, L. Linden Levy, P. Petreczky, R. Soltz, and P. Vranas for discussions. This work was performed under the auspices of the US Department of Energy by Lawrence Livermore National Laboratory under Contract No. DE-AC52-07NA27344 and was also supported in part by National Science Foundation Grant No. NSF PHY-0555660.

---

[1] R. Vogt, Eur. Phys. J. ST **155**, 213 (2008).
[2] M. Cacciari, P. Nason, and R. Vogt, Phys. Rev. Lett. **95**, 122001 (2005).
[3] R. Gavai, D. Kharzeev, H. Satz, G. A. Schuler, K. Sridhar, and R. Vogt, Int. J. Mod. Phys. A **10**, 3043 (1995).
[4] R. Vogt, Eur. Phys. J. C **61**, 793 (2009).
[5] P. Nason, S. Dawson, and R. K. Ellis, Nucl. Phys. B **303**, 607 (1988); **327**, 49 (1989).
[6] H. L. Lai, M. Guzzi, J. Huston, Z. Li, P. M. Nadolsky, J. Pumplin, and C.-P. Yuan, Phys. Rev. D **82**, 074024 (2010).
[7] C. McNeile, C. T. H. Davies, E. Follana, K. Hornbostel, and G. P. Lepage, Phys. Rev. D **82**, 034512 (2010).
[8] P. L. McGaughey, E. Quack, P. V. Ruuskanen, R. Vogt, and X.-N. Wang, Int. J. Mod. Phys. A **10**, 2999 (1995).
[9] N. Kidonakis, E. Laenen, S. Moch, and R. Vogt, Phys. Rev. D **67**, 074037 (2003).
[10] N. Kidonakis and R. Vogt, Eur. J. Phys. C **36**, 201 (2004).
[11] G. A. Alves *et al.* (E769 Collaboration), Phys. Rev. Lett. **77**, 2388 (1996).
[12] M. Aguilar-Benitez *et al.* (NA16 Collaboration), Phys. Lett. B **135**, 237 (1984).
[13] M. Aguilar-Benitez *et al.* (NA27 Collaboration), Z. Phys. C **40**, 321 (1988).
[14] M. C. Abreu *et al.* (NA38 Collaboration and NA50 Collaborations), Eur. Phys. J. C **14**, 443 (2000).
[15] R. Ammar *et al.* (E743 Collaboration), Phys. Rev. Lett. **61**, 2185 (1988).
[16] K. Kodama *et al.* (E653 Collaboration), Phys. Lett. B **263**, 573 (1991).
[17] I. Abt *et al.* (HERA-B Collaboration), Eur. Phys. J. C **52**, 531 (2007).
[18] M. Glück, E. Reya, and A. Vogt, Z. Phys. C **53**, 651 (1992).
[19] C. Lourenço and H. K. Wöhri, Phys. Rep. **433**, 127 (2006).
[20] A. Adare *et al.* (PHENIX Collaboration), Phys. Rev. Lett. **97**, 252002 (2006).
[21] J. Adams *et al.* (STAR Collaboration), Phys. Rev. Lett. **94**, 062301 (2005).
[22] Y. Zhang *et al.* (STAR Collaboration), J. Phys. G **38**, 124142 (2011).
[23] L. Adamczyk *et al.* (STAR Collaboration), Phys. Rev. D **85**, 092010 (2012).
[24] B. Abelev *et al.* (ALICE Collaboration), J. High Energy Phys. 07 (2012) 191.
[25] M. Cacciari, M. Greco, and P. Nason, J. High Energy Phys. 05 (1998) 007; M. Cacciari, S. Frixione, and P. Nason, *ibid.* 03 (2001) 006.
[26] W. Beenakker, W. L. van Neerven, R. Meng, G. A. Schuler, and J. Smith, Nucl. Phys. B **351**, 507 (1991).
[27] M. Cacciari and M. Greco, Nucl. Phys. B **421**, 530 (1994).
[28] M. Cacciari (private communication).
[29] J. D. Richman and P. R. Burchat, Rev. Mod. Phys. **67**, 893 (1995).
[30] B. Abelev *et al.* (ALICE Collaboration), Phys. Lett. B **708**, 265 (2012).
[31] M. Cacciari, S. Frixione, N. Houdeau, M. L. Mangano, P. Nason, and G. Ridolfi, JHEP 10 (2012) 137.
[32] B. Abelev *et al.* (ALICE Collaboration), J. High Energy Phys. 01 (2012) 128.
[33] M. Schmelling and P. Spradlin (LHCb Collaboration), LHCb-CONF-2010-013.
[34] V. D. Barger, W. Y. Keung, and R. J. Phillips, Phys. Lett. B **91**, 253 (1980).
[35] V. D. Barger, W. Y. Keung, and R. J. Phillips, Z. Phys. C **6**, 169 (1980).
[36] J. F. Amundson, O. J. P. Eboli, E. M. Gregores, and F. Halzen, Phys. Lett. B **390**, 323 (1997).
[37] G. A. Schuler and R. Vogt, Phys. Lett. B **387**, 181 (1996).
[38] F. Maltoni *et al.*, Phys. Lett. B **638**, 202 (2006).
[39] A. Bamberger *et al.*, Nucl. Phys. B **134**, 1 (1978).
[40] M. J. Corden *et al.* (WA39 Collaboration), Phys. Lett. B **98**, 220 (1981).
[41] Yu. M. Antipov *et al.*, Phys. Lett. B **60**, 309 (1976).
[42] K. J. Anderson *et al.*, Phys. Rev. Lett. **36**, 237 (1976); **37**, 799 (1976).
[43] J. Badier *et al.* (NA3 Collaboration), Z. Phys. C **20**, 101 (1983).
[44] J. G. Branson *et al.* (E331 Collaboration), Phys. Rev. Lett. **38**, 1331 (1977).
[45] K. J. Anderson *et al.* (E444 Collaboration), Phys. Rev. Lett. **42**, 944 (1979).
[46] L. Antoniazzi *et al.* (E705 Collaboration), Phys. Rev. D **46**, 4828 (1992).
[47] C. Morel *et al.* (UA6 Collaboration), Phys. Lett. B **252**, 505 (1990).
[48] H. D. Snyder *et al.* (E288 Collaboration), Phys. Rev. Lett. **36**, 1415 (1976).
[49] E. J. Siskind *et al.* (E595 Collaboration), Phys. Rev. D **21**, 628 (1980).

[50] M. C. Abreu *et al.* (NA51 Collaboration), Phys. Lett. B **438**, 35 (1998).

[51] M. C. Abreu *et al.* (NA38 Collaboration), Phys. Lett. B **444**, 516 (1998).

[52] B. Alessandro *et al.* (NA50 Collaboration), Eur. Phys. J. C **33**, 31 (2004).

[53] A. Gribushin *et al.* (E672/706 Collaboration), Phys. Rev. D **62**, 012001 (2000).

[54] T. Alexopoulos *et al.* (E771 Collaboration), Phys. Rev. D **55**, 3927 (1997).

[55] M. H. Schub *et al.* (E789 Collaboration), Phys. Rev. D **52**, 1307 (1995).

[56] I. Abt *et al.* (HERA-B Collaboration), Phys. Lett. B **638**, 407 (2006).

[57] J. H. Cobb *et al.*, Phys. Lett. B **68**, 101 (1977).

[58] C. Kourkoumelis *et al.*, Phys. Lett. B **91**, 481 (1980).

[59] A. G. Clark *et al.*, Nucl. Phys. B **142**, 29 (1978).

[60] E. Nagy *et al.*, Phys. Lett. B **60**, 96 (1975).

[61] E. Amaldi *et al.*, Lett. Nuov. Cim. **19**, 152 (1977).

[62] S. S. Adler *et al.* (PHENIX Collaboration), Phys. Rev. Lett. **92**, 051802 (2004).

[63] S. Eidelmann *et al.*, Phys. Lett. B **592**, 1 (2004).

[64] M. J. Leitch *et al.* (E866 Collaboration), Phys. Rev. Lett. **84**, 3256 (2000).

[65] C. Lourenço, R. Vogt, and H. Wöhri, J. High Energy Phys. 02 (2009) 014.

[66] R. Arnaldi *et al.* (NA60 Collaboration), Phys. Lett. B **706**, 263 (2012).

[67] M. L. Mangano, P. Nason, and G. Ridolfi, Nucl. Phys. B **373**, 295 (1992).

[68] A. D. Frawley, T. Ullrich, and R. Vogt, Phys. Rep. **462**, 125 (2008).

[69] D. Acosta *et al.* (CDF Collaboration), Phys. Rev. D **71**, 032001 (2005).

[70] A. Adare *et al.* (PHENIX Collaboration), Phys. Rev. D **85**, 092004 (2012).

[71] M. L. Mangano, P. Nason, and G. Ridolfi, Nucl. Phys. B **405**, 507 (1993).

[72] K. Aamodt *et al.* (ALICE Collaboration), Phys. Lett. B **704**, 442 (2011); **718**, 692(E) (2012).

[73] B. Abelev *et al.* (ALICE Collaboration), Phys. Lett. B **718**, 295 (2012).